

Tropical Atlantic decadal oscillation and its impact on the equatorial atmosphere-ocean dynamics: A simple model study

S.-K. Lee¹ and C. Wang²

¹ Cooperative Institute for Marine and Atmospheric Studies, University of Miami, Miami FL

² Atlantic Oceanographic and Meteorological Laboratory, NOAA, Miami FL

Submitted to Journal of Physical Oceanography
May 2006 (revised)

Abstract. Simple atmosphere-ocean coupled models are used to study the potential impact of the tropical Atlantic decadal oscillation on the equatorial atmosphere-ocean dynamics. Perturbing the model tropical Atlantic at the extra-tropics ($25\text{-}30^\circ$) with a decadal frequency, inter-hemispheric SST dipole mode emerges due to the Wind-Evaporation-SST feedback. Near the equator, the cross-equatorial oceanic gyre circulation develops due to the dipole-induced wind stress curl. In turn, this oceanic gyre transports surface water across the equator from the cold to the warm hemisphere in the western boundary region and from the warm to the cold hemisphere in the Sverdrup interior. Interestingly, this happens during both the positive and negative phases of the dipole oscillation, thus, producing a persistent positive zonal SST gradient along the equator (the nonlinear vertical mixing also contributes to the positive zonal SST gradient). Bjerknes-type feedback later kicks in to further strengthen the equatorial SST anomaly. This feature eventually grows to a quasi-stationary stage sustaining the equatorial westerly wind anomalies; thus, also causing the depression (uplift) of the equatorial thermocline in the east (west), a condition similar to the permanent Atlantic-Niño. The dynamic relationship between the dipole SST oscillation and the equatorial thermocline suggests that a strengthening (weakening) of the dipole mode corresponds to a weakening (strengthening) of the equatorial thermocline slope.

1. Introduction

Unlike the tropical Pacific, climatic fluctuations over the tropical Atlantic are largely forced by perturbations of remote origins, such as El Niño-Southern Oscillation (ENSO) and North Atlantic Oscillation (NAO) (Curtis and Hastenrath, 1995; Nobre and Shukla, 1996; Enfield and Mayer, 1997; Czaja et al. 2002; Enfield et al. 2006). Tropical Atlantic variability (TAV) includes two major modes, namely the Atlantic-Niño and dipole modes (a preferable terminology for the latter is cross-equatorial SST gradient mode, or simply meridional mode, but here we use these terms interchangeably). The first mode is analogous to ENSO in the Pacific and prevails at the interannual time scale, but requires external perturbations to sustain finite-amplitude oscillations (Zebiak, 1993). The second mode, on the other hand, is dominant at the decadal time scale and the associated SST anomaly is most pronounced off the equator around 10-15° latitude bands (Chang et al., 1997; Xie, 1999). Like the Atlantic-Niño mode, the meridional mode is weakly damped (Xie, 1999), thus anti-symmetric configurations of SST anomaly are not ubiquitous in the tropical Atlantic (Enfield et al. 1999). Nevertheless, using a semi-empirical model for the relationship between surface heat flux and SST, Chang et al. (1997) find that the interactions of the ocean and atmosphere through surface heat flux give rise to decadal oscillations of dipole structure similar to observations (*e.g.*, Nobre and Shukla, 1996). Consistent with this finding, Xie (1999) demonstrates clearly that a dipole SST pattern can emerge in a simple atmosphere-ocean coupled model of the tropical Atlantic through the Wind-Evaporation-SST (WES) feedback (Xie and Philander, 1994), if the extra-tropical decadal forcing is robust. Collectively, these studies suggest that the Atlantic dipole mode is not self-sustaining, thus it is critically dependent upon the extra-tropical forcing patterns. But, many of these studies also suggest that, even in the absence of inter-hemispheric SST anti-correlation, significant (more than 95% confidence) cross-

equatorial SST gradients occur frequently (about 50% of the time during 1856-1991 according to Enfield et al. 1999) and can be associated with climate variability in the tropical Atlantic region (Wang, 2002). A recent Coupled General Circulation Model (CGCM) study by Huang and Shukla (2005) also shows that the WES feedback can prevail in non-dipole configurations, causing mid-latitude disturbances to propagate equatorward, in agreement with idealized model studies (Liu, 1996; Xie, 1997). See Xie and Carton (2004) for a complete review on patterns, mechanisms and climate impacts of TAV.

It has been suggested that tropical ocean dynamics do not have a major impact on TAV (Carton et al. 1996; Seager et al. 2001; Alexander and Scott, 2002; Chang et al., 2003; Barreiro et al. 2005; Saravanan and Chang, 2004; Joyce et al. 2004). However, some studies argue that the equatorial Atlantic Ocean dynamics are actively involved in TAV. Servain et al. (1999; 2000), for instance, report that a significant correlation exists between the two tropical Atlantic modes at both the decadal and interannual time scales during 1979-93, and that both modes involve latitudinal displacements of the ITCZ as in the annual response. Murtugudde et al. (2001) present a partially supportive modeling result stressing that the two modes are significantly correlated only for limited record lengths prior to and after 1976. They argue that the correlation falls apart when longer time-series from 1949 to 2000 are considered, due to the large shift in equatorial thermocline depth that occurred in late 1970s. They also suggest that the meridional mode is strong prior to the large shift in equatorial thermocline depth but it weakens afterwards, while the opposite is true for the zonal mode.

These recent findings of Servain et al. (1999; 2000) and Murtugudde et al. (2001) generate many important questions that deserve further investigations. Among others, one key question that we want to explore in this study is *how the meridional SST oscillation and the equatorial*

atmosphere-ocean dynamics are potentially tied together at the decadal or longer time scales. Since the internal variability in the equatorial Atlantic is preferred at the interannual time scale (Zebiak, 1993), it is unlikely that the meridional mode is significantly affected by the equatorial atmosphere-ocean dynamics at the decadal or longer time scales. Therefore, our working hypothesis is that the equatorial atmosphere-ocean dynamics can be influenced or even controlled by the dipole SST oscillation at the decadal or longer time scales. We test this hypothesis by performing a series of simple coupled model experiments. It will be shown in the following sections that this hypothesis is indeed valid and that the cross-equatorial gyre circulation and the associated nonlinear heat advection play a key role in bridging the meridional SST oscillation and the equatorial atmosphere-ocean dynamics.

The framework of our modeling study closely follows Xie (1999). Here, we revise and extend his model by allowing zonal variations in both atmosphere and ocean, and replacing the slab ocean model with a fully dynamic 2.5-layer reduced gravity ocean model previously used in Lee and Csanady (1999).

2. Models

The original Gill (1980) model is used for the atmosphere. The governing equations are written as (unless specified otherwise, all variables are perturbations from their mean states)

$$\varepsilon U - fV = -\frac{\partial P}{\partial x}, \quad (2.1)$$

$$\varepsilon V + fU = -\frac{\partial P}{\partial y}, \quad (2.2)$$

$$\varepsilon P + C^2 \left(\frac{\partial U}{\partial x} + \frac{\partial V}{\partial y} \right) = -KT_1, \quad (2.3)$$

where U and V are the zonal and meridional components of lower tropospheric wind perturbation, P is the lower tropospheric pressure anomaly (divided by air density), T_1 is the SST anomaly, f is the Corioles parameter, C is the internal gravity wave speed, ε is the damping rate and K is the thermal coupling coefficient.

The ocean model is a 2.5-layer reduced gravity model (Lee and Csanady, 1999) consisting of two active layers, the surface mixed layer and the thermocline layer, on top of the stagnant deep layer. The momentum and continuity equations, linearized from the mean state, can be written as

$$\frac{\partial \mathbf{v}_1}{\partial t} - \mathbf{f} \mathbf{k} \times \mathbf{v}_1 = -\frac{1}{\rho_0} \nabla p_1 + \frac{c_d \mathbf{V}}{\rho_0 H_1} + A_h \nabla^2 \cdot \mathbf{v}_1, \quad (2.4)$$

$$\frac{\partial \mathbf{v}_2}{\partial t} - \mathbf{f} \mathbf{k} \times \mathbf{v}_2 = -\frac{1}{\rho_0} \nabla p_2 + A_h \nabla^2 \cdot \mathbf{v}_2, \quad (2.5)$$

$$\frac{\partial h_1}{\partial t} + H_1 \nabla \cdot \mathbf{v}_1 = w_e, \quad (2.6)$$

$$\frac{\partial h_2}{\partial t} + H_2 \nabla \cdot \mathbf{v}_2 = -w_e, \quad (2.7)$$

where \mathbf{v}_1 and \mathbf{v}_2 are the anomalous velocity vectors for the two active layers, h_1 and h_2 are the thickness perturbations from their mean values H_1 and H_2 , \mathbf{V} is the surface wind perturbation vector, c_d is the drag coefficient and A_h is the horizontal momentum diffusion coefficient. On the basis of the hydrostatic relation, the pressure gradient terms are given by

$$\nabla p_1 = g \alpha \nabla [h_1 (\bar{T}_1 - \bar{T}_3) + h_2 (\bar{T}_2 - \bar{T}_3)], \quad (2.8)$$

$$\nabla p_2 = g \alpha \nabla [(h_1 + h_2) (\bar{T}_2 - \bar{T}_3)], \quad (2.9)$$

where α is the thermal expansion coefficient, \bar{T}_1 , \bar{T}_2 and \bar{T}_3 are mean state temperatures of the two active layers and the deep inert layer, respectively. The anomalous vertical entrainment rate, w_e , is parameterized as linearly dependent on the mixed layer depth anomaly, h_1 :

$$w_e = -\gamma h_1, \quad (2.10)$$

where the vertical mixing coefficient γ is set to $(365\text{day})^{-1}$. It is important to note that this equation is used for estimating anomalous entrainment rate, not the total. Therefore, a negative value does not necessarily mean detrainment, but it rather means a reduction of entrainment rate due to the deepening of mixed layer.

The thermodynamic equation for the mixed layer, which is used to compute the SST anomaly (T_1), can be written as

$$\begin{aligned} \frac{\partial T_1}{\partial t} + \left(\bar{\mathbf{v}}_1 \cdot \nabla T_1 + \mathbf{v}_1 \cdot \nabla \bar{T}_1 + \underbrace{\mathbf{v}_1 \cdot \nabla T_1}_{(i)} \right) &= \frac{\bar{Q}_e}{c_p \rho_0 H_1} \left(\frac{\bar{U}U + \bar{V}V}{\bar{U}^2 + \bar{V}^2} \right) - rT_1 \\ &\quad - \underbrace{\frac{w_e}{H_1} (\bar{T}_1 + T_1 - \bar{T}_2)}_{(ii)} + A_T \nabla^2 T_1 + F, \end{aligned} \quad (2.11)$$

where the overbar denotes the mean state variable, c_p is the specific heat of sea water, r is the thermal damping coefficient, A_T is the thermal diffusion coefficient, \bar{Q}_e is the latent heat flux of the mean state (positive downward), \bar{U} and \bar{V} are the zonal and meridional surface wind component of the mean state, respectively, and F is the external forcing to be described later. Note that the temperatures of the lower layers remain constant (*i.e.*, $T_2 = T_3 = 0$), thus no additional equation is needed for the thermocline layer. The three terms inside the bracket on the lhs of (2.11) are advective heat flux divergence terms. It is assumed that the mean state is motionless and has a constant mixed layer temperature, thus the first two terms inside the bracket vanish and the only remaining term is (i) the nonlinear advective heat flux divergence. The first term on the rhs of (2.11) is obtained by linearizing the bulk formula for latent heat flux (see Liu, 1996 and Xie, 1999 for detailed derivation), and it is the central component for the WES feedback to occur in the coupled model. The second term on the rhs is the thermal damping term

arising from temperature dependence of latent heat flux. The third term is (ii) the vertical mixing and the fourth term is the thermal diffusion.

The model Atlantic domain is a rectangular box, extending zonally from 80°W to 20°E and meridionally from 30°S to 30°N with the model resolution of about 0.7°. The north and south boundaries are closed with a slip-condition applied at all sidewalls. The Gill atmospheric model also extends from 30°S to 30°N, but it is a global model in zonal direction with a periodic boundary condition. The mean ocean state is 200m deep ($H_1=100\text{m}$; $H_2=100\text{m}$) with the thermal parameters chosen to yield two internal gravity wave speeds of 2.5 and 1.0 ms^{-1} . All model parameters and their values used in this study are listed in Table 1. These values in the table are chosen to be identical to those used in Xie (1999) except for three parameters, namely the thermal coupling coefficient, K , the thermal damping coefficient, r and the drag coefficient, c_d . These values are appropriately chosen to ensure that the simulated WES feedback is weakly damped in the tropical Atlantic model configuration with an intrinsic resonant period at approximately 10 years, as indicated in previous observational and modeling studies.

In order to mimic the decadal extra-tropical perturbations typically caused by the NAO, SST perturbations are imposed only between 25° and 30° in both hemispheres, with the forcing period of 10 years. Coupled model runs are carried out using an anti-symmetric extra-tropical forcing pattern, *i.e.*, the sign of forcing is opposite in the two hemispheres but with the same amplitude, thus the forcing term F in (2.11) is given by

$$F = \begin{cases} \kappa \cdot \cos(2\pi/10\text{yrs} \cdot t) & \text{for } y = 25^\circ \text{N} - 30^\circ \text{N} \\ 0 & \text{for } y = 25^\circ \text{S} - 25^\circ \text{N} \\ -\kappa \cdot \cos(2\pi/10\text{yrs} \cdot t) & \text{for } y = 25^\circ \text{S} - 30^\circ \text{S}, \end{cases} \quad (2.12)$$

where κ is set to $1^\circ\text{C} (365\text{day})^{-1}$.

Five primary experiments are carried out with and without one of the two thermodynamic terms that involve ocean dynamics (*i.e.*, i and ii in 2.11). In the first experiment (Exp-1), the Gill atmospheric model is coupled to a so-called slab ocean model. In this case, the two terms that involve ocean dynamics are neglected in (2.11). In the second experiment (Exp-2), a coupled model run is carried out by including (i) the nonlinear advective heat flux divergence while neglecting (ii) the vertical mixing term. Similarly, (ii) the vertical mixing term is included but (i) the nonlinear advection term is excluded in the third and fourth experiments (only the linear portion of the vertical mixing is included in Exp-3 while only the nonlinear portion is included Exp-4). Finally, in the fifth experiment (Exp-5), both terms that involve ocean dynamics (i and ii) are included. In all of these experiments, the WES feedback (*i.e.*, the first term on the rhs of 2.11), thermal damping, thermal diffusion and forcing terms are retained. In the following section, these five coupled model runs under the anti-symmetric extra-tropical forcing (2.12) are used to describe the potential impact of the dipole oscillation on the equatorial atmosphere-ocean system.

3. Results

a. Thermally coupled experiment

The first experiment is performed by coupling the Gill atmosphere with the slab ocean model (*i.e.*, the two terms that involve ocean dynamics are neglected in 2.11). Fig. 1(a), (b) and (c) show the latitude-time structure of the zonally averaged SST anomaly and wind anomaly components, respectively. The structure of the solution closely resembles the WES feedback mode studied earlier (Xie, 1999), showing clearly the SST see-saw pattern north and south of the equator that slowly propagates equatorward, and the cross-equatorial winds blowing from the

cold to the warm hemisphere. As explained by Liu (1996), the equatorial propagation can be understood as follows. A warm SST anomaly in the tropics produces a westerly wind anomaly on the equator side and an easterly wind anomaly on the poleward side. The westerly wind anomaly reduces the mean trade wind speed while the easterly wind anomaly increases the mean wind speed. Accordingly, the related latent heat flux anomaly induces warming on the equator side and cooling on the poleward side, thus causing the warm SST anomaly to propagate toward the equator.

Fig. 1(d), (e) and (f) show the latitude-time structure of the zonally averaged mixed layer depth anomaly and surface ocean current anomaly components corresponding to the wind stress forcing shown in Fig. 1(b) and (c). Note that the ocean anomalies shown here are simply forced by the dipole-induced wind stress, thus, they are not actively involved in the atmosphere-ocean coupling. The mixed layer depth anomaly (h_1) and the SST anomaly (T_1) are negatively correlated, with the former lags the later by about 3 ~ 4 years; thus, the mixed layer depth is more likely to be shallower in the warm hemisphere and deeper in the cold hemisphere, in agreement with earlier studies (*e.g.*, Joyce et al., 2004). The zonal transport anomaly (u_1H_1), which has the maximum amplitude around 5° , is mainly controlled by the Sverdrup dynamics. The net cross-equatorial transport anomaly (v_1H_1) is, on the other hand, entirely related to the mixed layer depth oscillation (h_1) through the continuity equation because there is no mass flux into or out of the model domain. Generally, it is in the direction from the warming (*i.e.*, $\partial T_1/\partial t > 0$) hemisphere to the cooling hemisphere (*i.e.*, $\partial T_1/\partial t < 0$). The cross-equatorial gyre transport and the related ocean dynamics are explored further in the later part of this section.

Fig. 2(a) shows the two-dimensional structure of SST and wind anomalies averaged for the positive phase (warm in the north and cold in the south), and Fig. 2(b) for the negative phase

(cold in the north and warm in the south) between the model year 21 and 30. As shown in Fig. 2(c), the dipole index used for the phase averaging is the area-averaged SST anomaly of the northern hemisphere from that of the southern hemisphere. It is important to be reminded that the model solution is not a standing oscillation: the model solution propagates toward the equator, as shown in Fig. 1, but the propagating solution is averaged out in Fig. 2. The structure of the oscillating solution shown in Fig 2(a) and (b) is very similar to the zonally uniform solution of Xie (1999), but anomalous SST and winds are more pronounced toward the west. As previously noted by Xie (1996), this feature appears to originate from westward propagating WES waves that amplify as they move westward.

Fig. 2(d) and (e) display oceanic mixed layer depth (h_1) and transport (u_1H_1 and v_1H_1) anomalies averaged between the model year 21 and 30 for the negative phase (shallow in the north and deep in the south), and for the positive phase (deep in the north and shallow in the south), respectively. As shown in Fig. 2(f), the dipole index used for the phase averaging is the area-averaged mixed layer depth anomaly of the northern hemisphere minus that of the southern hemisphere. As discussed earlier, the mixed layer depth anomaly (h_1) is negatively correlated with the SST anomaly (T_1), thus the mixed layer depth is more likely to be shallower in the warm hemisphere and deeper in the cold hemisphere. However, the most striking feature in Fig. 2(d) and (e) is the cross-equatorial gyre circulation that emerges due to the dipole-induced wind stress curl pattern (Joyce et al. 2004). Obviously, this gyre circulation plays no role in this case because the thermodynamic terms associated with ocean dynamics are all turned off. However, it will be shown in the next experiment (Exp-2) that when (i) the oceanic heat advection term is activated in the thermodynamic equation (2.11), this gyre circulation allows a cross-equatorial transport of the mixed layer water from the cold to the warm hemisphere in the western boundary region and

from the warm to cold hemisphere in the Sverdrup interior, thus, producing a positive SST gradient along the equator. But, before we move on to the next section, we want to explore the ocean dynamic processes that are responsible for the net cross-equatorial transport oscillation shown in Fig. 1(f). Note that the Ekman transport, $v_{\text{ekm}} = c_d U (\rho_0 f H_1)^{-1}$, is a significant portion of the net cross-equatorial transport as shown in Fig. 3(a), but the non-Ekman transport is stronger than the Ekman transport as illustrated in Fig. 3(b). Interestingly, the non-Ekman transport is 90° out of phase with the Ekman transport, suggesting that the non-Ekman transport is an ocean dynamic response that tends to compensate the inter-hemispheric mass-imbalance caused by the Ekman transport.

In the classical model of a wind-driven gyre circulation in a closed domain, the meridional mass transport in the Sverdrup interior is exactly balanced by the reverse transport in the western boundary region; thus, the net meridional mass transport below the Ekman layer vanishes at all latitudes (*e.g.*, Munk, 1950). However, as correctly pointed by Csanady (1986), the so-called “leak-proof” wind-driven gyre circulation models hide some important details of the wind-driven flow, notably the mass balance between wind drift in a surface Ekman layer and the non-Ekman transport below. Since the classical wind-driven model does not explain the net non-Ekman cross-equatorial transport shown in Fig. 3(b), here we use the framework of the so-called *cross-gyre transport solution* of Csanady (1986). Following this framework, the mixed layer transport is decomposed into nonvortical (potential flow) and nondivergent (solenoidal flow) components:

$$\begin{aligned}
 u_1 H_1 &= -\frac{\partial \phi_1}{\partial x} - \frac{\partial \psi_1}{\partial y} , \\
 v_1 H_1 &= -\frac{\partial \phi_1}{\partial y} + \frac{\partial \psi_1}{\partial x} ,
 \end{aligned}
 \tag{3.1}$$

where ϕ_1 is the transport potential and ψ_1 is the stream function. The divergence and curl of transport can be written as

$$\begin{aligned}\nabla^2 \phi_1 &= -H_1 \left(\frac{\partial u_1}{\partial x} + \frac{\partial v_1}{\partial y} \right), \\ \nabla^2 \psi_1 &= H_1 \left(\frac{\partial v_1}{\partial x} - \frac{\partial u_1}{\partial y} \right).\end{aligned}\tag{3.2}$$

The boundary conditions are $\partial\phi/\partial\mathbf{n} = 0$ and $\psi = 0$ at all side walls, where \mathbf{n} is the unit vector normal to each sidewall. With these boundary conditions, the two Poisson equations (3.2) can be solved using the method of successive over relaxation, given the divergence and vorticity from the model output. By definition, the solenoidal flow component ($v_{\text{sol}}H_1 = \partial\psi_1/\partial x$) contributes nothing to the net cross-equatorial transport, thus the net cross-equatorial transport shown in Fig. 1(f) is exclusively due to the potential flow component ($v_{\text{pot}}H_1 = -\partial\phi_1/\partial y$).

Fig. 4(a) and (b) show the stream function (ψ_1) and solenoidal flow ($u_{\text{sol}}H_1$ and $v_{\text{sol}}H_1$) anomalies for the mixed layer averaged between the model year 21 and 30 for the positive phase, and the negative phase, respectively. The dipole index used for the phase averaging is the area-averaged zonal solenoidal transport anomaly ($u_{\text{sol}}H_1$) of the northern hemisphere minus that of the southern hemisphere as shown in Fig. 4(c). A close inspection of Fig. 4(a) and (b) along with Fig. 2(d) and (e) indicates that the oceanic response to the dipole-induced wind stress forcing can be largely explained by using the classical theory of a nondivergent wind-driven gyre circulation (Munk, 1950).

Fig. 4(d) and (e) display transport potential (ϕ_1) and potential flow ($u_{\text{pot}}H_1$ and $v_{\text{pot}}H_1$) anomalies for the mixed layer averaged between the model year 21 and 30 for the positive phase and the negative phase, respectively. As shown in Fig. 4(f), the dipole index used for the phase

averaging is the area-averaged transport potential anomaly of the northern hemisphere minus that of the southern hemisphere. Two striking features are noted. First, the potential flow has no boundary current component. Second, the cross-equatorial potential flow is 90° out of phase with the solenoidal flow, that is, when the potential flow is maximized, the cross-equatorial gyre circulation disappears (or change the sign of rotation).

The main lesson in the work of Csanady (1986) is that cross-gyre transport is needed to satisfy the mass imbalance caused by the Ekman transport, and that the cross-gyre transport involves nonvortical flows, thus, it is usually concealed in the classical wind-driven circulation models. The dynamics of potential flow in this case are somewhat different from the original cross-gyre transport solution, which is applicable only for steady state flows. Thus, in the original cross-gyre transport model, Ekman pumping is the only source of divergence that drives the potential flow. In this case, however, two additional sources of divergence are the local rate of change of the mixed layer depth and the entrainment from the thermocline layer, as clearly indicated in the continuity equation of mixed layer (2.6). A consorted influence of the three divergence sources determines the amplitude and phase of net cross-equatorial transport.

In summary, this experiment (Exp-1) confirms that extra-tropical perturbations could cause meridional SST oscillation in the tropical Atlantic through thermodynamic feedback (Xie, 1999), and that the dipole-induced wind forcing could drive a cross-equatorial gyre circulation (Joyce et al., 2004). Further analyses suggest that the cross-equatorial gyre circulation is largely explained by using the classical theory of wind-driven gyre circulation (Munk, 1950), but the net cross-equatorial transport is not. The cross-gyre transport solution of Csanady (1986) provides a useful insight to explain the ocean dynamics that regulate the net cross-equatorial mass transport.

b. The role of oceanic heat advection

In this experiment (Exp-2), a coupled model run is performed by including (i) the nonlinear advective heat flux divergence term in the thermodynamic equation (2.11). Fig. 5(a) and (b) are the same as in Fig 2(a) and (b) but for the Exp-2. The dipole index used for the phase averaging is the area-averaged SST anomaly of the northern hemisphere from that of the southern hemisphere, as shown in Fig 5c (thin solid line). The most striking departure from the previous experiment is the infiltration of the warm hemisphere into the cold hemisphere in the interior ocean, and the opposite trend in the western boundary region. As a result, a positive (negative) zonal SST anomaly gradient persists in the western (eastern) equatorial ocean during both the positive and negative phases of the dipole oscillation. A close inspection of Fig. 5(c) indicates that during the positive dipole phase between the model year 22 and 26, the cross-equatorial gyre is an anti-clockwise in the first year, but it switches to a clockwise circulation for the remaining 4 years (the area-averaged zonal transport of the northern hemisphere minus that of the southern hemisphere is used as the index for cross-equatorial gyre circulation; thus, a negative index value indicates an anti-clockwise circulation and a positive value indicates a clockwise circulation). Hence, a clockwise cross-equatorial gyre circulation prevails during the positive SST dipole phase. Similarly, an anti-clockwise cross-equatorial gyre circulation prevails during the negative SST dipole phase. As a result, the cross-equatorial gyre circulation transports mixed layer water from the cold to the warm hemisphere in the western boundary region and from the warm to the cold hemisphere in the Sverdrup interior. Since this happens during both the positive and negative phases of the dipole oscillation, a persistent cold anomaly is produced in the western boundary region and a warm anomaly in the Sverdrup interior. Another noticeable feature in Fig. 5(a) and (b) is the zonal shifts of the SST anomaly maximum (eastward) and minimum

(westward). Again, the heat advection by the cross-equatorial gyre circulation is accountable for this model feature: in association with the cross-equatorial gyre circulation, the westward current anomaly in the cold hemisphere presses the SST anomaly minimum toward west while the eastward current anomaly in the warm hemisphere carries the SST anomaly maximum toward the east.

An important implication of these results is that, when ocean dynamics (heat advection in particular) are allowed to participate in the dipole oscillation, a permanent shift may occur in the zonal structure of the equatorial atmosphere and ocean. To better describe the role of oceanic heat advection and the associated equatorial shift, it is useful to look at the time-averaged model solution: shown in Fig. 6(a) are the two-dimensional structures of SST and wind anomalies averaged for one full cycle of the dipole oscillation between the model year 21 and 30. The positive SST anomaly in the central equatorial ocean is due to the cross-equatorial gyre circulation and the related meridional heat advection as discussed earlier. The wind anomaly pattern is a typical Gill atmosphere response to an isolated heating source at the central equatorial ocean: a damped (atmospheric) Kelvin wave along the equator with the zonal wind converging toward the heating source, and a damped (atmospheric) Rossby wave off the equator (Gill, 1980).

Fig. 6(b) shows mixed layer depth (h_1) and transport (u_1H_1 and v_1H_1) anomalies averaged for the same period between the model year 21 and 30. The shallow thermocline depth and eastward transport anomalies in the western equatorial ocean are consistent with the westerly wind anomaly there. It is important to note that the changes in the thermocline depth do not make direct impact on the SST anomaly because (ii) the vertical mixing term is excluded in this

experiment; thus, the equatorial positive feedback, also known as Bjerknes feedback (Bjerknes, 1969), does not play any role here.

Heat advection is neither a source nor a sink of thermal energy, because it merely redistributes thermal energy between different geographic locations. Accordingly, the amplitude and phase of the dipole oscillation are minimally affected by the oceanic heat advection as it becomes clear by comparing the dipole index of this experiment (Fig. 5(c)) from that of the previous experiment (Fig. 2(c)). Nevertheless, the cross-equatorial gyre circulation and the related heat advection generate some interesting model features, in particular the expansion of the warm hemisphere into the cold hemisphere in the Sverdrup interior and vice versa in the western boundary region. A warm SST anomaly is then created in the central equatorial ocean, and persists during both the positive and negative phases of the dipole oscillation. In turn, this equatorial SST anomaly forces the Gill atmosphere to produce westerly wind anomaly in the western equatorial ocean. In response to this wind anomaly, the shallow thermocline depth and eastward transport anomalies persist in the western equatorial ocean. Since the vertical mixing is turned off, the Bjerknes feedback does not play a role in this experiment.

c. The role of vertical mixing

In this subsection, we want to understand how the vertical mixing influences the dipole oscillation. For this, the vertical mixing term in the thermodynamic equation is divided into the linear and nonlinear terms:

$$-\frac{w_e}{H_1}(\bar{T}_1 + T_1 - \bar{T}_2) = -\frac{w_e}{H_1}(\bar{T}_1 - \bar{T}_2) - \frac{w_e}{H_1}T_1. \quad (3.3)$$

Two experiments are carried out. In one experiment (Exp-3), only the linear vertical mixing term (the first term in the rhs of 3.3) is included in the thermodynamic equation (2.11), and in the

other experiment (Exp-4), only the nonlinear vertical mixing term (the second term in the rhs of 3.3) is included. Fig. 7 is the same as in Fig. 1 but for the Exp-3. When the model solution is compared to the thermally coupled case (Exp-1), it is noted that the amplitude of dipole oscillation is reduced considerably (note that different contour intervals are used in Fig. 1 and Fig. 7), suggesting that the mixed layer depth oscillation and the related linear vertical mixing contribute to a negative feedback. The dynamics responsible for this negative feedback is very straightforward. Fig. 7(a) and (d) reveal that the mixed layer depth anomaly (h_1) is negatively correlated with the SST anomaly (T_1) without much time lag; thus the mixed layer depth is shallower in the warm hemisphere and deeper in the cold hemisphere. Because the linear vertical mixing is proportional to the mixed layer depth anomaly (see 2.10 and 3.3), it tends to cool down the warm hemisphere and to warm up the cold hemisphere, a negative feedback mechanism.

Comparing Fig. 7 with Fig. 1, it is also noted that the equatorward propagation of SST anomaly is much faster in Exp-3. In the thermally coupled case (Exp-1), it takes about 3.5 years for a SST anomaly signal to propagate from 30°N to the equator, but it takes only about 2 years when the linear vertical mixing is turned on. By comparing Fig. 7(a) and (d), it is noted that the mixed layer depth anomaly is slightly shifted poleward of the SST anomaly by about 2 degrees or more. This means that the mixed layer depth anomaly and the related linear vertical mixing tend to cool off (warm up) the poleward side of warm (cold) SST anomaly more effectively than the equator side. It appears that the enhanced cooling (warming) poleward side of the warm (cold) SST anomaly facilitates the equatorward propagation of the SST anomaly. The two-dimensional structure of the model solution for Exp-3 is very similar to as in Fig. 2, but with much reduced amplitude, thus, it is not shown here.

In the next experiment (Exp-4), the nonlinear vertical mixing term (the second term in the rhs of 3.3) is included in the thermodynamic equation (2.11) instead of the linear vertical mixing term. Fig. 8 is the same as in the left column of Fig. 2 but for Exp-4. In comparison to the thermally coupled case (Exp-1), one distinctive feature shown in Fig. 8 is that the cold hemisphere is intensified while the warm hemisphere is weakened. Fig 8(c) clearly shows that the SST and mixed layer depth anomalies are negatively correlated, with no apparent time lag. Since the nonlinear vertical mixing is proportional to $T_1 h_1$ (see 2.10 and 3.3), it contributes to a cooling in both hemispheres; thus, weakening the warm hemisphere and strengthening the cold hemisphere during both the positive and negative phases of the dipole oscillation.

While the horizontal heat advection term is excluded in this experiment, the structure of the model solution shares two important features of the Exp-2 (Fig. 5). First, the SST minimum is pushed against the western boundary while the SST maximum is shifted to the east. To explain this feature, it is important to recognize that the amplitude of mixed layer depth anomaly is pronounced off the western boundary due to beta effect (Stommel, 1948). Therefore, the nonlinear vertical mixing and the related cooling are also maximized off the western boundary region causing the intensification of SST minimum and weakening of the SST maximum there. This explains why the SST minimum is pushed against the western boundary while the SST maximum is shifted to the east. Another important feature to note is that the cold hemisphere infiltrates the warm hemisphere in the western side of model ocean, and vice versa in the interior equatorial ocean. Heat budget analysis suggests that the horizontal heat diffusion causes the expansion of the cold hemisphere into the warm hemisphere in the western side of the model ocean where the predominance of the cold hemisphere is most pronounced (not shown). Fig. 9, which is the same as in Fig. 6 but for Exp-4, further shows that the nonlinear vertical mixing

together with the heat diffusion produces a positive zonal SST gradient along the equator causing a westerly wind anomaly over the central equatorial ocean. This equatorial wind anomaly in turn causes the mixed layer deepening in the eastern equatorial ocean. Near the western boundary, cold SST anomalies prevail because the cold hemisphere predominates the warm hemisphere there. This also explains why the easterly wind anomaly persists in the western boundary region.

In summary, we find that the linear vertical mixing tends to decrease the amplitude of dipole oscillation and to facilitate the equatorial movement of extra-tropical SST anomalies. But, the most important conclusion is that the equatorial system is undisturbed by the linear vertical mixing. The nonlinear vertical mixing, on the other hand, does influence the equatorial system, and the characteristics of the model solution are surprisingly similar to those with the oceanic heat advection. In particular, the nonlinear vertical mixing produces a positive zonal SST gradient and a westerly wind anomaly along the equator. The predominance of the cold hemisphere to the warm hemisphere is another noticeable impact of the nonlinear vertical mixing.

d. The integrated effect of ocean dynamics

So far, we have been exploring the individual role of heat advection, linear vertical mixing and nonlinear vertical mixing in the dipole oscillation by performing three coupled model experiments that allow only one of the three processes in each experiment. However, since these ocean dynamic processes coexist in reality, we next explore the role of the integrated ocean dynamics in the dipole oscillation by performing a fully coupled model experiment (Exp-5) – all terms in the thermodynamic equation (2.11) are included in this experiment. In all our previous model experiments, the coupled simulations arrive at their equilibriums after about 10 years or

so. In this fully coupled case, however, the basin-averaged energy grows for an extended period of more than several decades until the model reaches a quasi-equilibrium stage.

Before we explore why the fully coupled system takes longer time to adjust, it is helpful to first look at the two-dimensional structure of the solution: Fig. 10 is the same as in the left column of Fig. 2 but for Exp-5. In comparison to the thermally coupled case (Exp-1), the off-equatorial amplitude of the dipole oscillation is significantly reduced as in Exp-3, apparently due to the damping effect of linear vertical mixing (See Fig. 10(c)). As in Exp-2 and Exp-4, the positive zonal SST gradient persists in the western and central equatorial oceans due to the influence of heat advection and nonlinear vertical mixing. Therefore, it appears that the fully coupled model experiment (Exp-5) contains all the major characteristics of Exp-2, Exp-3 and Exp-4 indicating that all three ocean dynamic processes, heat advection (Exp-2), linear vertical mixing (Exp-3) and nonlinear vertical mixing (Exp-4), work more or less independently. But, this conclusion does not apply in the eastern basin where the strong warm SST anomaly prevails with its maximum centered at the equator. Since the warm SST anomaly persists during both the positive and negative phases of the dipole oscillation, it is useful to look at the time-averaged model solution: Fig. 11 is the same as in Fig. 9 but for this experiment (Exp-5). It is apparent that the equatorial SST anomaly has much larger amplitude than those shown in Fig. 6 (Exp-2) or Fig. 9 (Exp-4), and it is most intense in the eastern equatorial ocean. The presence of an intensified equatorial SST anomaly indicates that a positive feedback is at work and it tends to amplify the positive zonal SST gradient along the equator, which is originally caused by the heat advection and nonlinear vertical mixing. The westerly wind and deepened thermocline anomalies in the eastern equatorial ocean suggest that the Bjerknes feedback plays an important role.

Further insight can be gained by using the following analogical model for the eastern equatorial SST anomaly, T_o :

$$\frac{dT_o}{dt} = aT_o - bT_o + c. \quad (3.4)$$

The first term in the rhs represents positive feedback with the growth rate a , mainly the Bjerknes feedback. The second term represents damping processes that limit the growth of instabilities (negative feedback), such as Newtonian damping. The third term represents the tendency (rate) of the fully coupled model to create a persistent positive zonal SST gradient anomaly along the equator, thus c is always positive. The solution to equation 3.4 is given by (the initial condition is $T_o = 0$)

$$T_o = \frac{c}{b-a}(1 - \exp[-(b-a)t]). \quad (3.5)$$

It is important to note that the damping rate is always larger than the growth rate, *i.e.*, $b - a > 0$, because the coupled system is stable without the forcing term, c . Therefore, the equilibrium solution ($T_o = c/(b - a)$; $t \rightarrow \infty$) is always a warm anomaly, and its magnitude depends critically on the damping rate minus growth rate, $(b - a)$. This solution also explains that an e -folding time of $(b - a)^{-1}$ is required for the system to adjust to the final equilibrium stage. In this particular experiment (Exp-5), the e -folding time is about several decades, but it varies with different parameter values that affect a , b and c .

In summary, the dipole-induced cross-equatorial gyre circulation and the related heat advection (together with the nonlinear vertical mixing) are directly responsible for inducing the positive zonal SST gradient along the equator, and the subsequent atmosphere-ocean positive feedback further intensifies the zonal SST gradient anomaly, eventually creating a condition similar to the permanent Atlantic-Niño. Once the coupled system reaches its equilibrium stage,

the equatorial SST anomaly structure becomes nearly stationary, feeding its energy from the WES feedback that in turn requires decadal perturbations from extra-tropics. Since the Bjerknes feedback in the Atlantic is a damped mode, a continuous forcing is required for the permanent Atlantic-Niño to maintain its strength; thus, the core mechanism can be referred to as a *forced Bjerknes feedback*.

4. Simulating the decadal TAV of the past 50 years

Murtugudde et al (2001) reported two important characteristics of the tropical Atlantic decadal variability in the past 50 years. First, the main mode of tropical Atlantic SST variability changes during the 1970s from a meridional SST gradient mode to a zonal mode. Second, this change is accompanied by a shift in the zonal slope of the equatorial Atlantic thermocline. Now, a question is whether our fully coupled model can reproduce these characteristics of the tropical Atlantic decadal variability of the past 50 years. To answer this question, we perform an additional experiment (Exp-6). As in Exp-5, all terms in the thermodynamic equation (2.11) are retained, but the anti-symmetric extra-tropical forcing (2.12) is replaced with the following:

$$F = \begin{cases} \lambda \cdot T_{NA} & \text{for } y = 25^\circ\text{N} - 30^\circ\text{N} \\ 0 & \text{for } y = 25^\circ\text{S} - 25^\circ\text{N} \\ \lambda \cdot T_{SA} & \text{for } y = 25^\circ\text{S} - 30^\circ\text{S}, \end{cases} \quad (4.1)$$

where λ is set to $(365\text{day})^{-1}$. T_{NA} is the area-averaged SST anomaly for the North Atlantic ($70^\circ\text{W} - 20^\circ\text{W}$; $25^\circ\text{N} - 30^\circ\text{N}$) and T_{SA} is for the South Atlantic ($60^\circ\text{W} - 10^\circ\text{E}$, $25^\circ\text{S} - 30^\circ\text{S}$). NCAR/NCEP atmospheric reanalysis SST data (Kalnay et al., 1996) is used to compute the two extra-tropical SST anomaly time series, T_{NA} and T_{SA} .

Fig. 12 shows the latitude-time evolution of the (a) simulated versus (b) observed (three-year running mean) SST anomaly between 20°S and 20°N . The model seems to capture some low-

frequency fluctuations of the observed SST anomaly, but there are many noticeable differences between the model result and the observation. In particular, the model shows a positive dipole phase before mid-1970s, followed by a negative dipole phase period between mid-1975s and late-1990s. This is consistent with the NAO phase shift that occurred around mid-1970s from a negative to a positive phase (Hurrell, 1995), but the observed SST anomalies are masked by much complicated oscillation patterns that are in many cases in non-dipole structure, particularly after the mid-1970s. The disagreement between the coupled model simulation and the observed SST anomaly suggests that the inter-hemispheric SST dipole oscillation explains only a portion of the tropical Atlantic decadal variability; thus, also reflecting the complexity of the tropical Atlantic decadal variability.

To obtain the equatorial Atlantic thermocline depth to be compared with the coupled model result, an OGCM simulation is carried out using a Hybrid Coordinate Ocean Circulation Model (HYCOM). The details on HYCOM configuration are documented in Lee et al. (2005), thus, they are summarized only briefly here. The model domain contains both the Pacific and Atlantic Oceans between 100°E and 20°E, bounded north and south by 65°N and 35°S, respectively. The grid resolution is uniform 1° zonally and variable in the meridional direction; 0.5° at the equator increasing linearly to 1° at 40° latitude and remaining 1° poleward of 40°. In the vertical, 22 non-uniform hybrid layers are used. The constrained Southampton surface flux climatology (Grist and Josey, 2003) is combined with the ECMWF 40-year global reanalysis data (Brankovic and Molteni, 2004) to force the HYCOM for the period of 1958-2001.

Shown in Fig. 13 is the longitude-time structure of (a) the equatorial mixed layer depth anomaly from the coupled model run, and (b) the 20°C isotherm depth anomaly in the equatorial Atlantic (three-year running mean) obtained from the HYCOM run. Since the extra-tropical

forcing in this case (4.1) contains a full spectrum of perturbations, with the forcing in the north more or less independent of that in the south, we do not expect that the coupled model behave as in the idealized model experiment (Exp-5). Indeed, our coupled model under the realistic forcing does not produce a permanent Atlantic-Niño. Instead, the model undergoes a decadal fluctuation, showing an interesting shift in the equatorial thermocline depth around mid-1980s. The OGCM simulation also shows a similar shift in the equatorial thermocline around late-1970s, in agreement with the earlier OGCM study of Murtugudde et al. (2001).

5. Summary and Discussions

Motivated by recent observations that the two tropical Atlantic climate modes (the zonal and meridional modes) are potentially related at the decadal time scale, we carry out a series of simple coupled model runs to understand the underlying physics, and our findings can be summarized as follows. Perturbing the model tropical Atlantic at the extra-tropics ($25\text{-}30^\circ$) with a decadal frequency, inter-hemispheric SST dipole mode emerges due to the WES feedback. Near the equator, a cross-equatorial gyre circulation develops due to the dipole-induced wind stress curl. This gyre circulation transports equatorial surface water from the cold to the warm hemisphere in the western boundary region and from the warm to the cold hemisphere in the Sverdrup interior. Since this happens during both positive and negative phases of the dipole oscillation, a positive zonal SST gradient persists along the equator (the nonlinear vertical mixing also contributes to the positive zonal SST gradient). Bjerknes feedback later kicks in to strengthen the equatorial SST anomaly. This feature eventually grows to a quasi-stationary stage sustaining the equatorial westerly wind anomalies, thus, also causing the depression (uplift) of

the equatorial thermocline in the east (west), a condition similar to the permanent Atlantic-Niño. A sketch that illustrates this mechanism is shown in Fig 14.

Although not shown here, additional experiments are performed with different extra-tropical forcing patterns. We find that the WES feedback mechanism still works under a symmetric extra-tropical forcing with and without ocean dynamics, but the oscillations are much weaker. The permanent Atlantic-Niño that prevails under the anti-symmetric extra-tropical forcing does not exist in that case. On the other hand, if the extra-tropical forcing is confined in the northern or southern hemisphere only, the permanent Atlantic-Niño does develop but with much reduced growth rate. These results suggest that inter-hemispheric SST contrast is the precondition for generating the permanent Atlantic-Niño.

It is a difficult task to fully validate our conclusions, particularly due to the complexity of the tropical Atlantic system where both the remotely forced and internally generated signals are mixed together. We also recognize the limitations of our coupled model involved in neglecting the seasonal mean flow effect and also the teleconnection from the equatorial Pacific (Latif and Grotzner, 2000). Due to many over-simplifications, our coupled model seems to have only a limited skill in reproducing the SST anomalies of the past 50 years. However, when driven only by the realistic extra-tropical forcing, our coupled model produces an interesting decadal fluctuation in the equatorial thermocline showing more or less similar pattern as in the OGCM simulation; thus, here we argue that the equatorial thermocline can be affected by the extra-tropical forcing through the atmosphere-ocean coupling (both thermal and dynamic). However, what we learn from the idealized model simulations does not fully explain this model behavior. This is because we consider only the anti-symmetric extra-tropical forcing with exactly 10 years of oscillation period, while the real extra-tropical forcing contains a full spectrum of

perturbations. In particular, it is rather surprising to note that the shallower-than-normal eastern equatorial thermocline depth anomaly lasts for an extended period from mid-1980s to 2001, because our coupled model under the idealized extra-tropical forcing does not explain this feature. To fully understand the model behavior under the realistic extra-tropical forcing, we need to perform many more model experiments using different extra-tropical forcings. Additionally, the effect of the pre-existing asymmetry of the seasonal mean flow must be fully explored because it may modify the cross-equatorial circulation gyre that plays the key role in bridging the meridional SST oscillation and the equatorial system. We are currently working to improve our coupled model in these respects.

Acknowledgements. This research was supported by a grant from NOAA Climate Program Office and by the base funding of NOAA/AOML. We are indebted to D. Enfield for many scientific discussions and encouragement. Comments from D. Enfield, A. Mestas-Nuñez and R. Molinari help improve the manuscript. We also thank two anonymous reviewers for their useful suggestions, which led to a significant improvement of the paper. The findings and conclusions in this report are those of the authors and do not necessarily represent the views of the funding agency.

References

- Alexander, M., and J. Scott, 2002: The influence of ENSO on air-sea interaction Atlantic, *Geophys. Res. Lett.*, 29, doi: 10.1029/2001GL014347.
- Barreiro, M., P. Chang, L. Ji, R. Saravanan and A. Giannini, 2005: Dynamical elements of predicting boreal spring tropical Atlantic sea-surface temperatures, *Dyn. Atmos. Oceans*, 39, 61-85.
- Bjerknes, J., 1969: Atmospheric teleconnections from the equatorial Pacific. *Mon. Wea. Rev.*, 97, 163-172.
- Brankovic, C. and F. Molteni, 2004: Seasonal climate and variability of the ECMWF ERA-40 model. *Climate Dyn.*, 22, 139-155.
- Carton, J. A., X. H. Cao, B. S. Giese, and A. M. da Silva, 1996: Decadal and interannual SST variability in the tropical Atlantic Ocean. *J. Phys. Oceanogr.*, 26, 1165-1175.
- Chang, P., L. Ji, and H. Li, 1997: A decadal climate variation in the tropical Atlantic Ocean from thermodynamic air-sea interactions. *Nature*, 385, 516-518.
- Chang, P., L. Ji, and R. Saravanan, 2001: A hybrid coupled model study of tropical Atlantic variability. *J. Clim.*, 14, 361-390.
- Chang, P., R. Saravanan, and L. Ji, 2003: Tropical Atlantic Seasonal Predictability: the Roles of El Niño remote influence and thermodynamic air-sea feedback. *Geophys. Res. Lett.*, 30, 1501-1504.
- Csanady, G. T., 1986: Cross-gyre transports. *J. Phys. Oceanogr.*, 16, 1703-1711.
- Curtis, S. and S. Hastenrath, 1995: Forcing of anomalous sea surface temperature evolution in the tropical Atlantic during Pacific warm events. *J. Geophys. Res.*, 100, 15835-15847.
- Czaja, A., P. Van der Vaart, and J. Marshall, 2002: A diagnostic study of the role of remote forcing in tropical Atlantic variability. *J. Clim.*, 15, 3280-3290.
- Enfield, D. B. and D. A. Mayer, 1997: Tropical Atlantic sea surface temperature variability and its relation to El Niño-Southern Oscillation. *J. Geophys. Res.*, 102, 929-945.
- Enfield, D. B., A. M. Mestas-Nuñez, D. A. Mayer, and L. Cid-Serrano, 1999: How ubiquitous is the dipole relationship in tropical Atlantic sea surface temperatures? *J. Geophys. Res.*, 104, 7841-7848.
- Enfield, D. B., S.-K. Lee, and C. Wang, 2006: How are large Western Hemisphere Warm Pools formed? *Progress in Oceanogr.*, (in press).
- Gill, A. E., 1980: Some simple solutions for heat-induced tropical circulation. *Quart. J. Roy. Meteor. Soc.*, 106, 447-462.
- Grist, J. P. and S. A. Josey, 2003: Inverse analysis adjustment of the SOC air-sea flux climatology using ocean heat transport constraints. *J. Climate*, 16, 3274-3295.
- Hurrell, J. W., 1995: Decadal trends in the North Atlantic Oscillation: Regional temperatures and precipitation, *Science*, 269, 676-679.
- Huang, B. and J. Shukla. 2005: Ocean-Atmosphere Interactions in the Tropical and Subtropical Atlantic Ocean. *J. Climate* 18, 1652-1672.
- Joyce, T. M., C. Frankignoul, J. Yang, H.E. Phillips, 2004: Ocean response and feedback to the SST dipole in the Tropical Atlantic. *J. Phys. Oceanogr.*, 34, 2525-2540
- Kalnay, E., M. Kanamitsu, R. Kistler, W. Collins, D. Deaven, L. Gandin, M. Iredell, S. Saha, G. White, J. Woollen, Y. Zhu, M. Chelliah, W. Ebisuzaki, W. Higgins, J. Janowiak, K. C. Mo, C. Ropelewski, J. Wang, Leetmaa, R. Reynolds, R. Jenne, and D. Joseph, 1996: The NCEP/NCAR 40-year Reanalysis Project. *Bull. American Meteorol. Soc.*, 77, 437-471.

- Latif, M., and A. Grotzner, 2000: The equatorial Atlantic oscillation and its response to ENSO. *Climate Dyn.*, 16, 213-218.
- Lee, S.-K., G. T. Csanady, 1999. Warm water formation and escape in the upper tropical Atlantic Ocean: 2. A numerical model study, *J. Geophys. Res.*, 104, 29,573 – 29,590.
- Lee, S.-K., D. B. Enfield, and C. Wang, 2005: Ocean general circulation model sensitivity experiments on the annual cycle of Western Hemisphere Warm Pool, *J. Geophys. Res.*, 110, C09004, doi:10.1029/2004JC002640
- Liu, Z. 1996: Modeling Equatorial Annual Cycle with a Linear Coupled Model. *J. Clim.*, 9, 2376-2385.
- Munk, W. H., 1950: On the wind driven ocean circulation., *J. Meteor.*, 7, 79-93.
- Murtugudde, R. G., J. Ballabrera-Poy, J. Beauchamp, A. J. Busalacchi, Relationship between zonal and meridional modes in the tropical Atlantic, *Geophys. Res. Lett.*, 28(23), 4463-4466, 10.1029/2001GL013407, 2001.
- Nobre, P. and J. Shukla, 1996: Variations of sea surface temperature, wind stress and rainfall over the tropical Atlantic and South America. *J. Clim.*, 9, 2464-2479.
- Saravanan, R. and P. Chang, 2004: Thermodynamic coupling and predictability of tropical sea surface temperature, In *Earth Climate: The Ocean-Atmosphere Interaction*, C. Wang, S.-P. Xie and J.A. Carton (eds.), *Geophys. Monogr.*, 147, AGU, Washington D.C., 171-180.
- Seager, R., Y. Kushnir, P. Chang, N. Naik, J. Miller and W. Hazeleger, 2001. Looking for the role of the ocean in tropical Atlantic decadal climate variability, *J. Clim.*, 14, 638-655.
- Servain, J. Jr., A. Dessier, Relationship between the equatorial and meridional modes of climatic variability in the tropical Atlantic, *Geophys. Res. Lett.*, 26(4), 485-488, 10.1029/1999GL900014, 1999.
- Servain, J. Jr., I. Wainer, H. L. Ayina, and H. Roquet, 2000. The relationship between the simulated climatic variability modes of the tropical Atlantic, *Internat. J. Clim.*, 20, 939 – 953.
- Stommel, H., 1948: The westward intensification of wind-driven ocean currents. *Trans. Am. Geophys. Union*, 29, 202-206.
- Wang, C., 2002. Atlantic climate variability and its associated atmospheric circulation cells, *J. Clim.*, 15, 1516 – 1536.
- Xie, S.-P., and S.G.H. Philander, 1994: A coupled ocean-atmosphere model of relevance to the ITCZ in the eastern Pacific, *Tellus*, 46A, 340-350.
- Xie, S.-P., 1996: Westward propagation of latitudinal asymmetry in a coupled ocean-atmosphere model. *J. Atmos. Sci.*, 53, 3236-3250.
- Xie, S.-P., 1997: Unstable Transition of the Tropical Climate to an Equatorially Asymmetric State in a Coupled Ocean-Atmosphere Model. *Mon. Wea. Rev.*, 125, 667-679.
- Xie, S.-P., 1999: A dynamic ocean-atmosphere model of the tropical Atlantic decadal variability. *J. Clim.*, 12, 64-70.
- Xie, S.-P. and J. A. Carton, 2004: Tropical Atlantic variability: Patterns, mechanisms, and impacts. *Earth Climate: The Ocean-Atmosphere Interaction*, C. Wang, S.-P. Xie and J.A. Carton (eds.), *Geophys. Monogr.*, 147, AGU, Washington D.C., 121-141.
- Zebiak, S. E., 1993. Air-sea interaction in the equatorial Atlantic region, *J. Clim.*, 6, 1567 – 1586.

Table 1. Model parameters and their values used for model integrations. ATM indicates parameters used for the atmospheric model, OCN for the ocean model and CPL for the atmosphere-ocean coupling, respectively.

Parameter	Notation	Value
ε^{-1}	inverse of damping rate (ATM)	2 days
K	thermal coupling coefficient (ATM)	$5.0 \times 10^{-3} \text{ m}^2 \text{ s}^{-3} \text{ K}^{-1}$
C	internal gravity wave speed (ATM)	45 m s^{-1}
\bar{U}	zonal wind speed of the mean state (ATM)	-4.5 m s^{-1}
\bar{V}	meridional wind speed of the mean state (ATM)	0 m s^{-1}
A_h	Laplacian mixing coefficient for momentum (OCN)	$2000 \text{ m}^2 \text{ s}^{-1}$
ρ_0	density of sea water (OCN)	1020 kg s^{-1}
c_p	specific heat of water (OCN)	$4200 \text{ m s}^{-2} \text{ K}^{-1}$
α	thermal expansion coefficient (OCN)	$2.5 \times 10^{-4} \text{ K}^{-1}$
γ^{-1}	inverse of vertical mixing coefficient (OCN)	1 year
H_1	thickness of the mixed layer (OCN)	100 m
H_2	thickness of the thermocline layer (OCN)	100 m
\bar{T}_1	mean state temperature of the mixed layer (OCN)	25°C
\bar{T}_2	mean state temperature of the thermocline layer (OCN)	20°C
\bar{T}_3	mean state temperature of the deep motionless layer (OCN)	15°C
\bar{Q}_e	latent heat flux of the mean state (positive downward) (CPL)	-125 W m^{-2}
r^{-1}	inverse of thermal damping coefficient (CPL)	1.9 years
c_d	drag coefficient (CPL)	$2 \times 10^{-2} \text{ N s m}^{-3}$
A_T	Laplacian mixing coefficient for heat (CPL)	$2000 \text{ m}^2 \text{ s}^{-1}$
κ	extra-tropical forcing coefficient (CPL)	1 year

Figure captions

Figure 1. Exp-1: Latitude-time structure of the zonally averaged (a) SST, (b) zonal wind, (c) meridional wind, (d) mixed layer depth, (e) zonal mixed layer transport and (f) meridional mixed layer transport anomalies. The unit is $^{\circ}\text{C}$ for the SST, ms^{-1} for the wind components, m for the mixed layer depth and m^2s^{-1} for the mixed layer transport components.

Figure 2. Exp-1: Two-dimensional structure of SST and wind anomalies averaged for (a) the positive phase and (b) the negative phase are shown in the left column. The dipole index used for the phase averaging is the area-averaged SST of the northern hemisphere minus that of the southern hemisphere as shown in (c). The mixed layer depth and transport anomalies averaged for (d) the negative phase and (e) the positive phase are shown in the right column. The dipole index used in this case is the area-averaged mixed layer depth of the northern hemisphere minus that of the southern hemisphere as shown in (f). The maximum wind is about 0.64 ms^{-1} , and the maximum mixed layer transport is about $16 \text{ m}^2\text{s}^{-1}$.

Figure 3. Exp-1: Latitude-time structure of the zonally averaged meridional (a) Ekman transport and (b) non-Ekman transport components. The unit is m^2s^{-1} . Ekman transport is not defined at the equator; thus, the transport values within the equatorial belt ($1^{\circ}\text{S} - 1^{\circ}\text{N}$) are not contoured.

Figure 4. Exp-1: The stream function (ψ_1) and solenoidal flow ($u_{\text{sol}}H_1$ and $v_{\text{sol}}H_1$) anomalies for the mixed layer averaged for (a) the positive phase and (b) the negative phase are shown in the left column. The dipole index used for the phase averaging is the area-averaged zonal solenoidal transport ($u_{\text{sol}}H_1$) of the northern hemisphere minus that of the southern hemisphere as shown in (c). The transport potential (ϕ_1) and potential flow ($u_{\text{pot}}H_1$ and $v_{\text{pot}}H_1$) anomalies for the mixed layer averaged for (d) the positive phase and for (e) the negative phase are shown in the right column. The dipole index used in this case is the area-averaged transport potential anomaly of the northern hemisphere minus that of the southern hemisphere as shown in (f). The unit is $10^{-6} \text{ m}^3\text{s}^{-1}$ for the stream function and transport potential, and m^2s^{-1} for the solenoidal flow and potential flow components. The maximum transport value is about $8.48 \text{ m}^2\text{s}^{-1}$ for the solenoidal flow component, and about $1.23 \text{ m}^2\text{s}^{-1}$ for the potential flow component.

Figure 5. Exp-2: Two-dimensional structure of SST and wind anomalies averaged for (a) the positive phase and (b) the negative phase. The dipole index used for the phase averaging is the area-averaged SST of the northern hemisphere minus that of the southern hemisphere as shown in (c). The broken line in (c) is the area-averaged zonal transport of the northern hemisphere minus that of the southern hemisphere, and this index is used for cross-equatorial gyre circulation: a negative value indicates a cyclonic circulation and a positive value indicates a clockwise circulation. The maximum wind is about 0.66 ms^{-1} .

Figure 6. Exp-2: The two-dimensional structures of (a) SST and wind anomalies, and (b) the mixed layer depth and transport anomalies, all averaged for one full cycle of the dipole oscillation between the model year 21 and 30. The maximum wind is about 0.17 ms^{-1} , and the maximum mixed layer transport is about $2.9 \text{ m}^2\text{s}^{-1}$.

Figure 7. Same as in Fig. 1 but for Exp-3. Note that the contour intervals are different from those used in Fig. 1.

Figure 8. Same as in the left column of Fig. 2 but for Exp-4. The broken line in (c) is the area-averaged mixed layer depth of the northern hemisphere minus that of the southern hemisphere. The maximum wind is about 0.75 ms^{-1} .

Figure 9. Same as in Fig. 6 but for Exp-4. The maximum wind is about 0.18 ms^{-1} , and the maximum mixed layer transport is about $3.0 \text{ m}^2\text{s}^{-1}$.

Figure 10. Same as in Fig. 8 but for Exp-5. The maximum wind is about 0.43 ms^{-1} .

Figure 11. Same as in Fig. 9 but for Exp-5. The maximum wind is about 0.25 ms^{-1} , and the maximum mixed layer transport is about $5.5 \text{ m}^2\text{s}^{-1}$.

Figure 12. Exp-6: Latitude-time evolution of the (a) simulated versus (b) observed SST anomaly (NCAR/NCEP reanalysis data; Kalnay et al., 1996), both averaged zonally between 80°W and 20°E . The observed SSTA is the three-year running mean.

Figure 13. Exp-6: Longitude-time structure of (a) the simulated equatorial mixed layer depth, and (b) the 20°C isotherm in the equatorial Atlantic obtained from the HYCOM run. In both cases, the depth anomalies are averaged between 5°S and 5°N . The HYCOM output is the three-year running mean.

Figure 14. Sketch of the mechanism by which the positive zonal SST gradient is induced along the equator during (a) the positive and (b) negative phases of the Atlantic dipole oscillation. Thicker arrows indicate wind perturbations associated with the dipole oscillation. Dark shades are used for warm SST anomalies and light shades for cold SST anomalies. W-D represents a warm and deep anomaly; W-S a warm and shallow anomaly; C-D a cold and deep anomaly; and C-S a cold and shallow anomaly. Closed circuits represent cross-equatorial gyre circulation that brings the tropical surface water toward the equator. This gyre circulation supplies cold water in the western boundary layer and warm water in the Sverdrup interior during both the positive and negative phases of the dipole oscillation. The warm equatorial SSTA is then shifted to the east and intensified as a result of the Bjerknes feedback, thus, producing a permanent Atlantic-Niño condition.

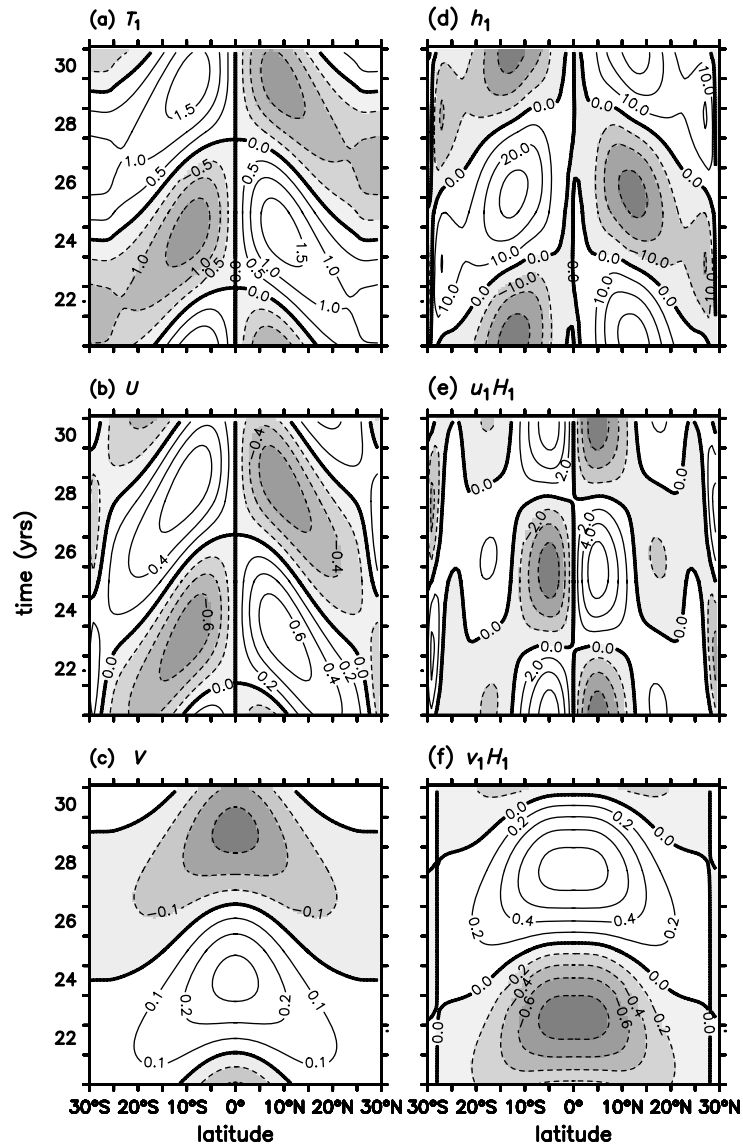


Figure 1. Exp-1: Latitude-time structure of the zonally averaged (a) SST, (b) zonal wind, (c) meridional wind, (d) mixed layer depth, (e) zonal mixed layer transport and (f) meridional mixed layer transport anomalies. The unit is $^{\circ}\text{C}$ for the SST, ms^{-1} for the wind components, m for the mixed layer depth and $\text{m}^2 \text{s}^{-1}$ for the mixed layer transport components.

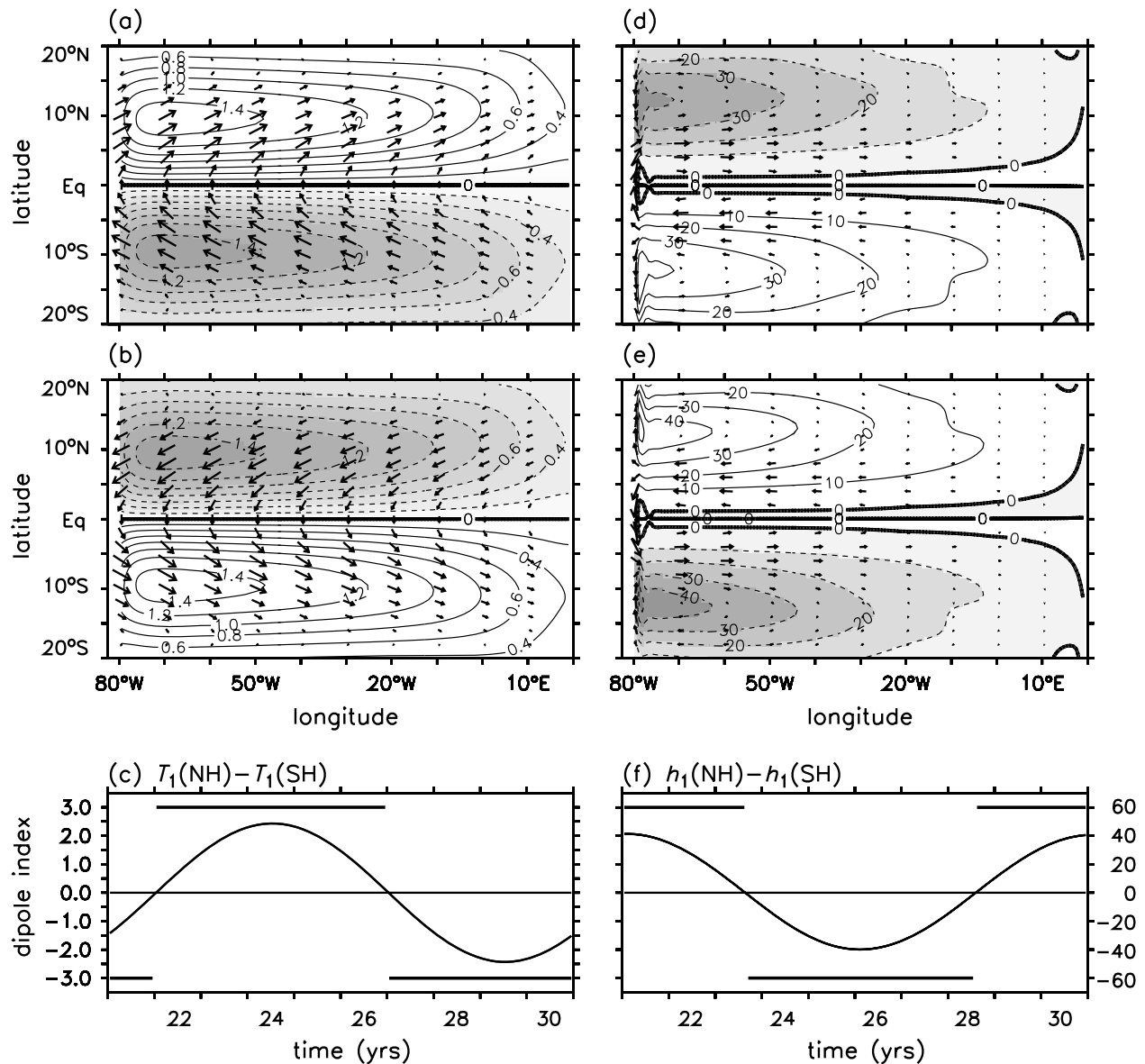


Figure 2. Exp-1: Two-dimensional structure of SST and wind anomalies averaged for (a) the positive phase and (b) the negative phase are shown in the left column. The dipole index used for the phase averaging is the area-averaged SST of the northern hemisphere minus that of the southern hemisphere as shown in (c). The mixed layer depth and transport anomalies averaged for (d) the negative phase and (e) the positive phase are shown in the right column. The dipole index used in this case is the area-averaged mixed layer depth of the northern hemisphere minus that of the southern hemisphere as shown in (f). The maximum wind is about $0.64 \text{ m}^2 \text{ s}^{-1}$, and the maximum mixed layer transport is about $16 \text{ m}^2 \text{ s}^{-1}$.

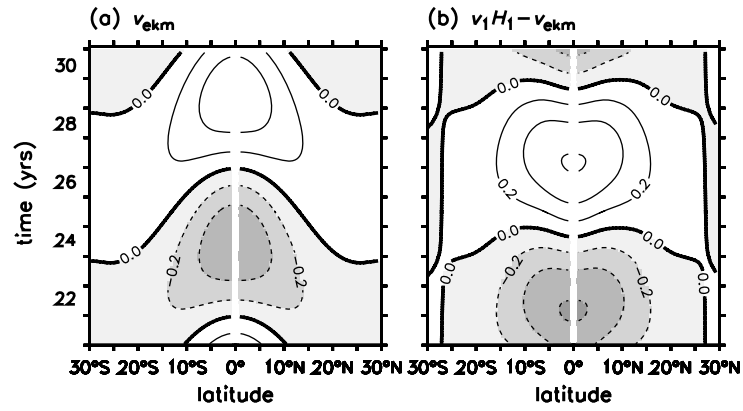


Figure 3. Exp-1: Latitude-time structure of the zonally averaged meridional (a) Ekman transport and (b) non-Ekman transport components. The unit is $\text{m}^2 \text{s}^{-1}$. Ekman transport is not defined at the equator; thus, the transport values within the equatorial belt ($1^\circ\text{S} - 1^\circ\text{N}$) are not contoured.

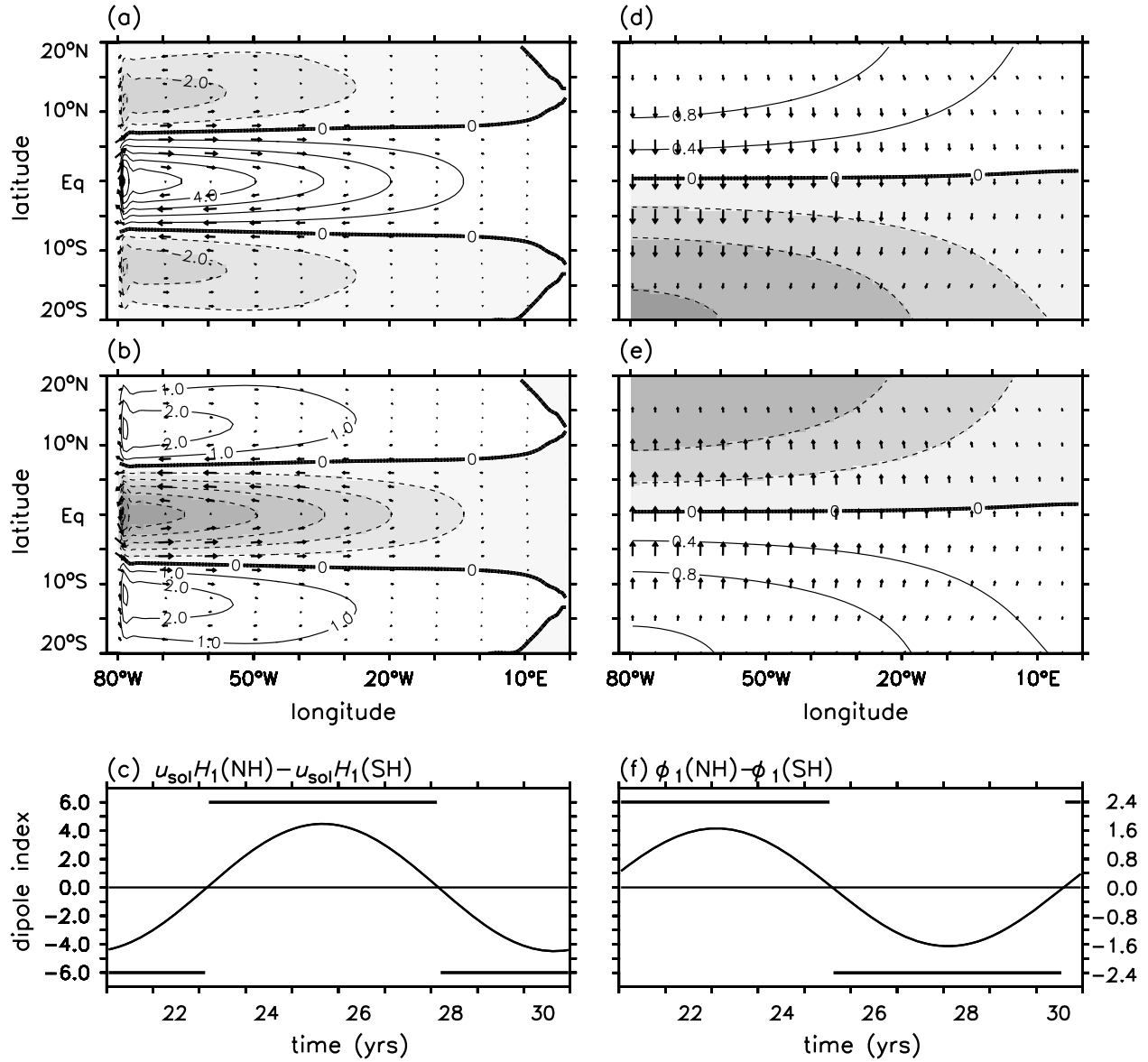


Figure 4. Exp-1: The stream function (ψ_1) and solenoidal flow ($u_{sol}H_1$ and $v_{sol}H_1$) anomalies for the mixed layer averaged for (a) the positive phase and (b) the negative phase are shown in the left column. The dipole index used for the phase averaging is the area-averaged zonal solenoidal transport ($u_{sol}H_1$) of the northern hemisphere minus that of the southern hemisphere as shown in (c). The transport potential (ϕ_1) and potential flow ($u_{pot}H_1$ and $v_{pot}H_1$) anomalies for the mixed layer averaged for (d) the positive phase and for (e) the negative phase are shown in the right column. The dipole index used in this case is the area-averaged transport potential anomaly of the northern hemisphere minus that of the southern hemisphere as shown in (f). The unit is $10^{-6} \text{ m}^3 \text{ s}^{-1}$ for the stream function and transport potential, and $\text{m}^2 \text{ s}^{-1}$ for the solenoidal flow and potential flow components. The maximum transport value is about $8.48 \text{ m}^2 \text{ s}^{-1}$ for the solenoidal flow component, and about $1.23 \text{ m}^2 \text{ s}^{-1}$ for the potential flow component.

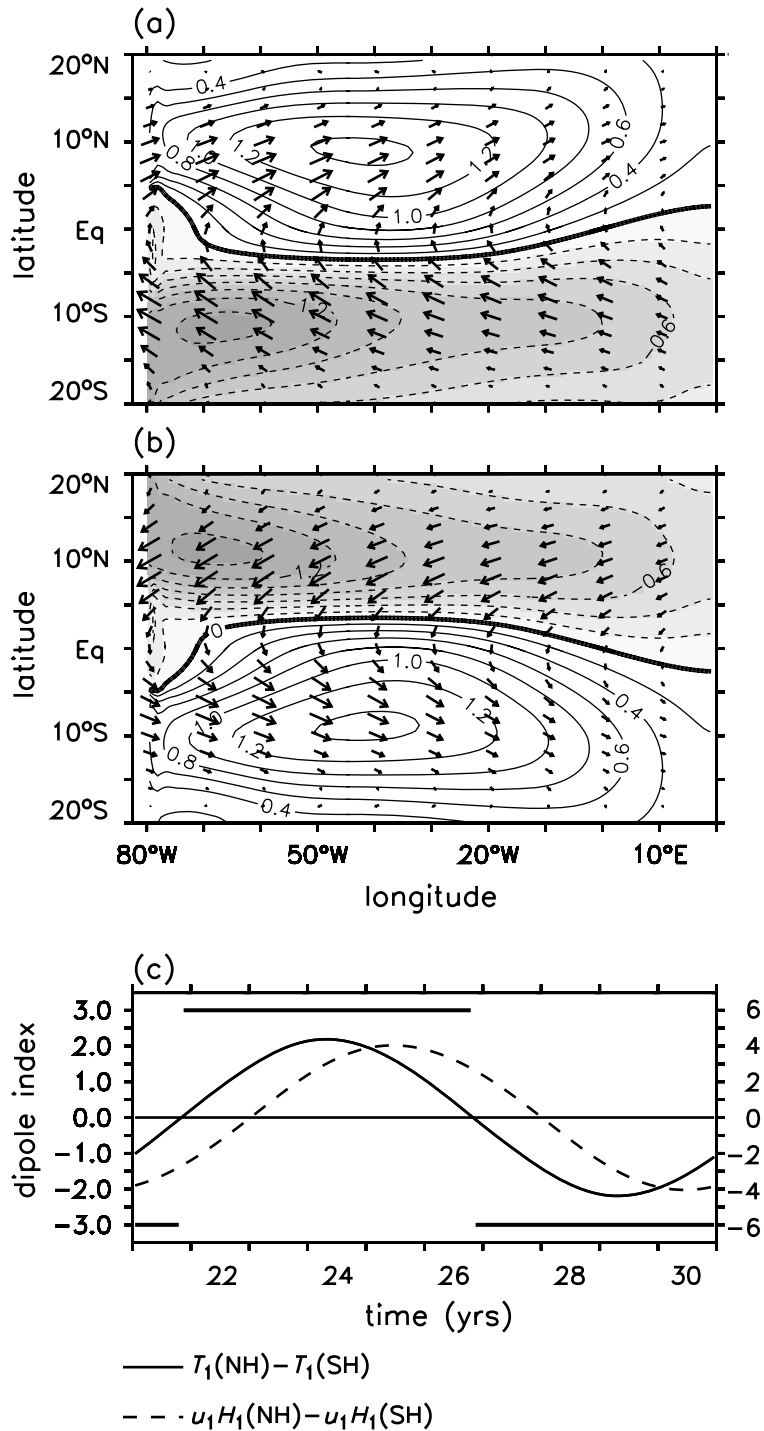


Figure 5. Exp-2: Two-dimensional structure of SST and wind anomalies averaged for (a) the positive phase and (b) the negative phase. The dipole index used for the phase averaging is the area-averaged SST of the northern hemisphere minus that of the southern hemisphere as shown in (c). The broken line in (c) is the area-averaged zonal transport of the northern hemisphere minus that of the southern hemisphere, and this index is used for cross-equatorial gyre circulation: a negative value indicates a cyclonic circulation and a positive value indicates a clockwise circulation. The maximum wind is about 0.66 ms^{-1} .

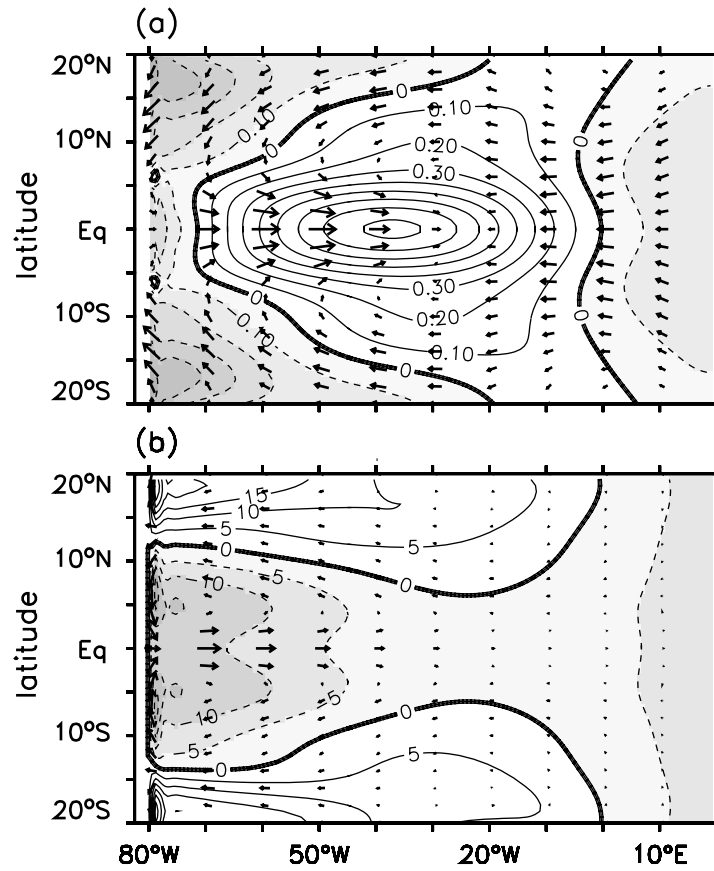


Figure 6. Exp-2: The two-dimensional structures of (a) SST and wind anomalies, and (b) the mixed layer depth and transport anomalies, all averaged for one full cycle of the dipole oscillation between the model year 21 and 30. The maximum wind is about 0.17 ms^{-1} , and the maximum mixed layer transport is about $2.9 \text{ m}^2 \text{ s}^{-1}$.

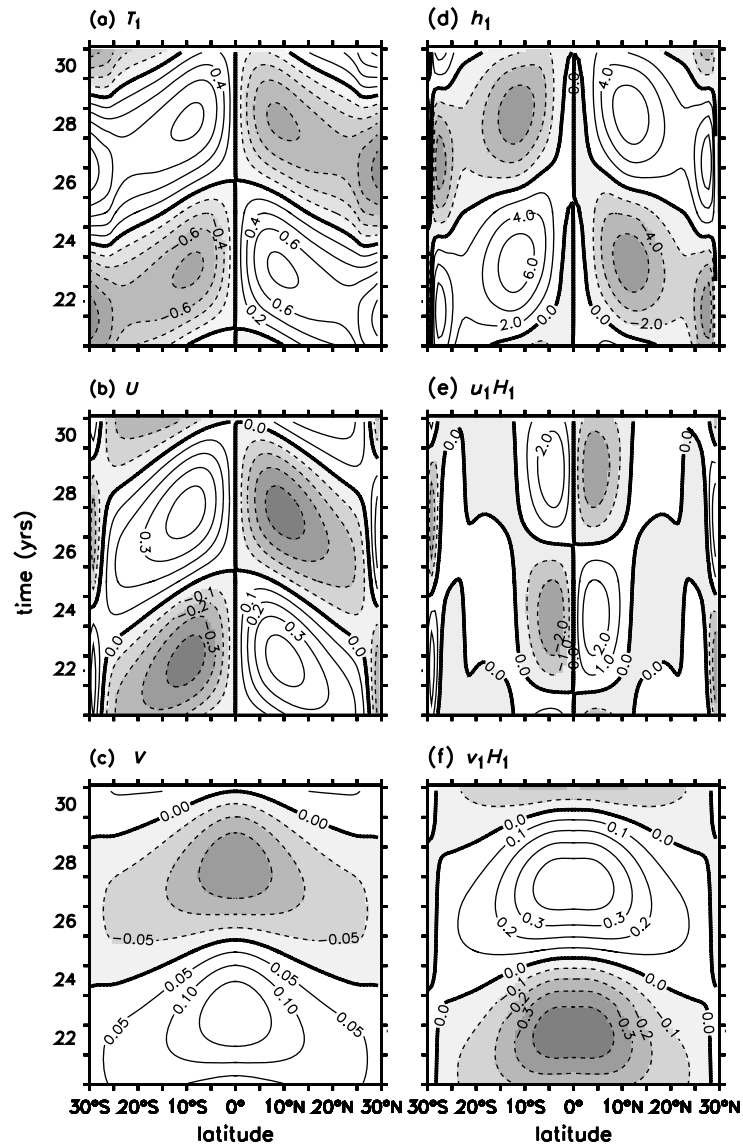


Figure 7. Same as in Fig. 1 but for Exp-3. Note that the contour intervals are different from those used in Fig. 1.

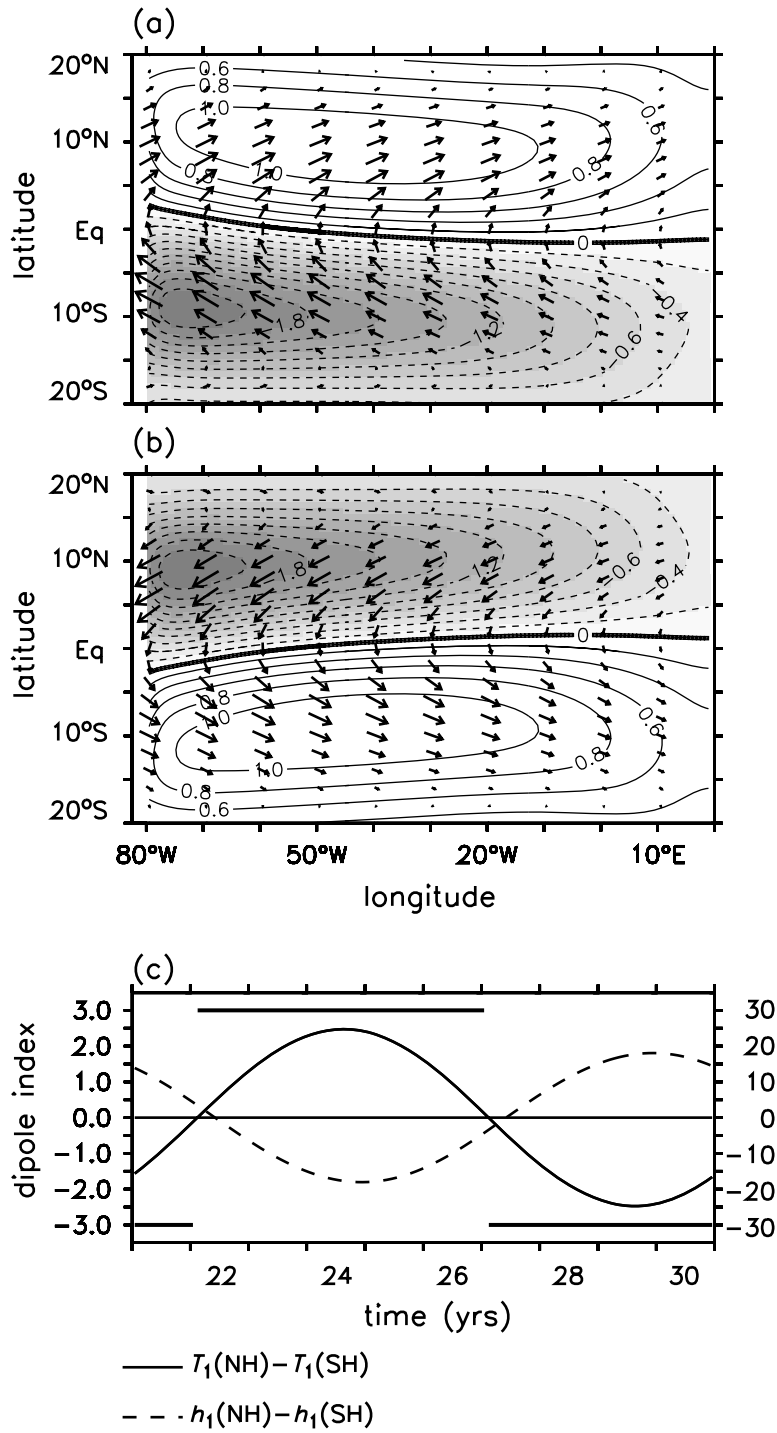


Figure 8. Same as in the left column of Fig. 2 but for Exp-4. The broken line in (c) is the area-averaged mixed layer depth of the northern hemisphere minus that of the southern hemisphere. The maximum wind is about 0.75 ms^{-1} .

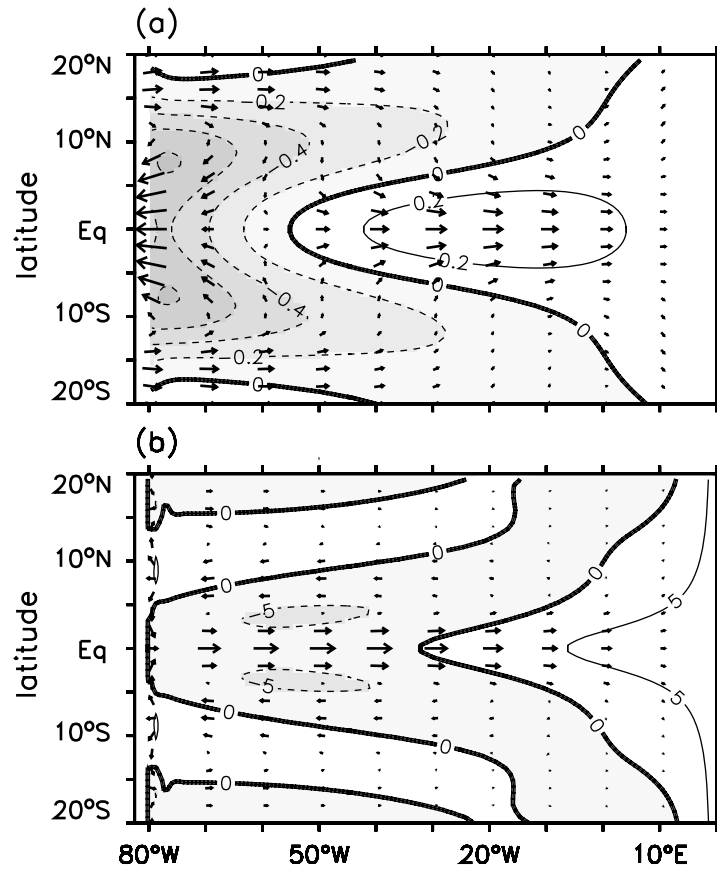


Figure 9. Same as in Fig. 6 but for Exp-4. The maximum wind is about 0.18 ms^{-1} , and the maximum mixed layer transport is about $3.0 \text{ m}^2 \text{ s}^{-1}$.

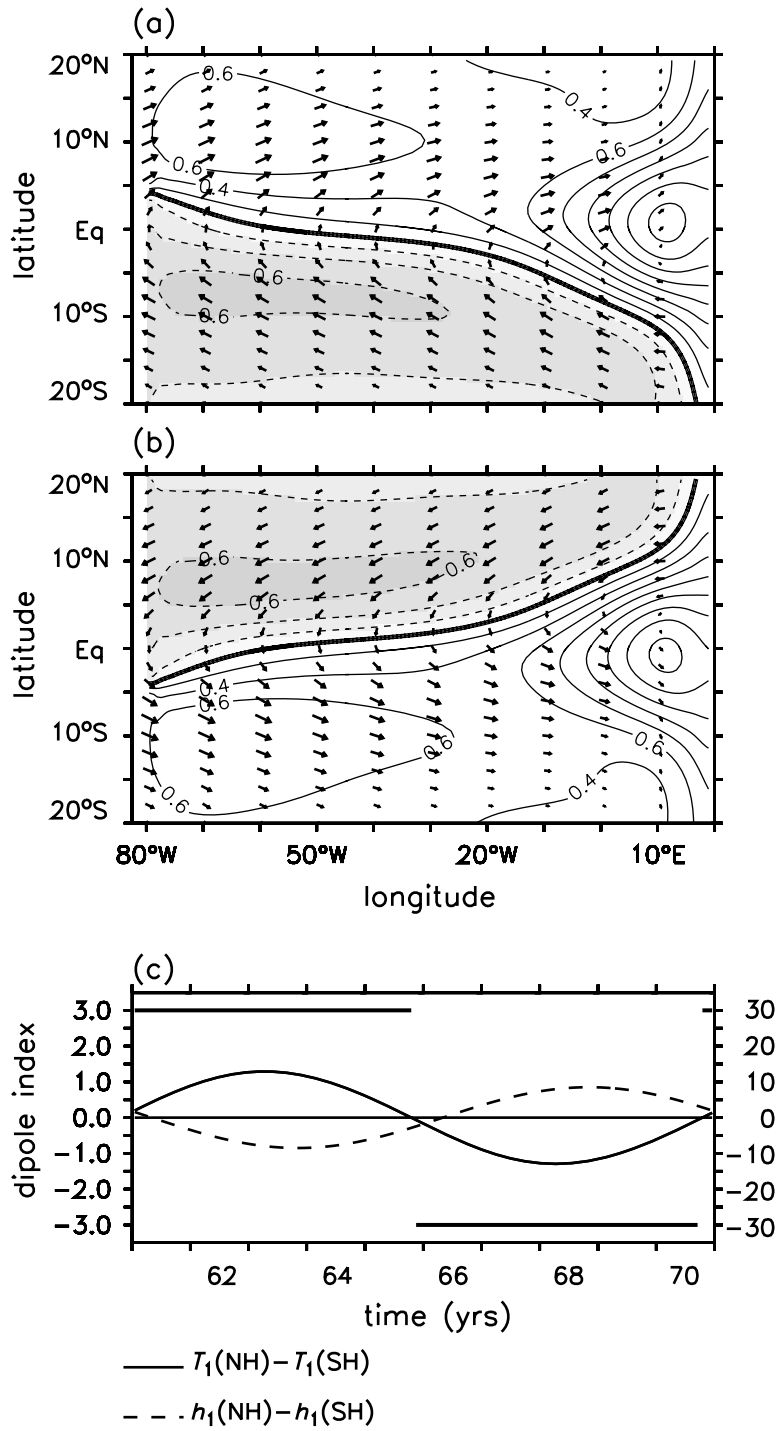


Figure 10. Same as in Fig. 8 but for Exp-5. The maximum wind is about 0.43 ms⁻¹.

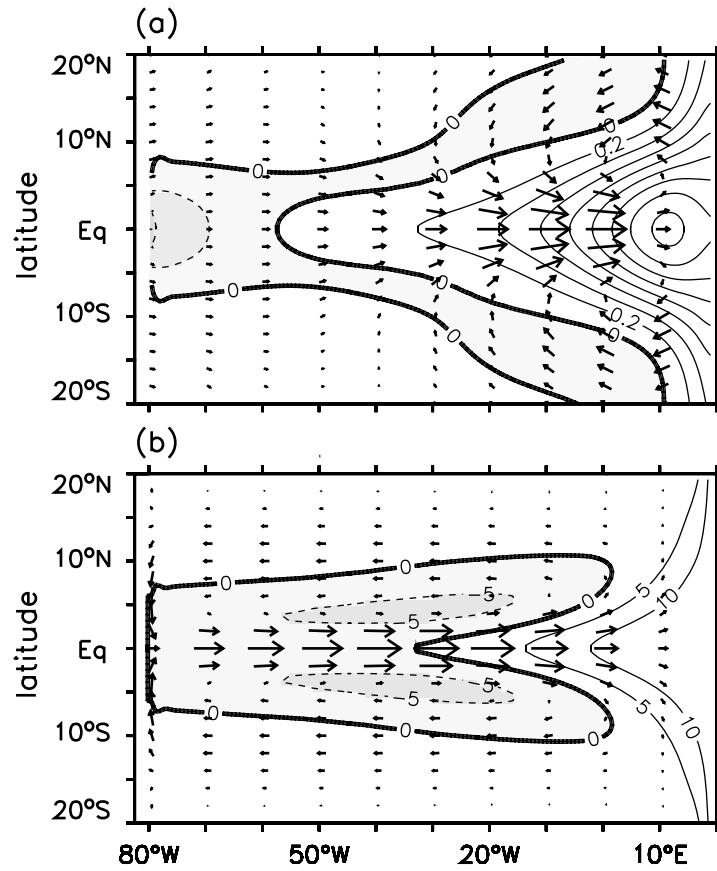


Figure 11. Same as in Fig. 9 but for Exp-5. The maximum wind is about 0.25 ms^{-1} , and the maximum mixed layer transport is about $5.5 \text{ m}^2 \text{ s}^{-1}$.

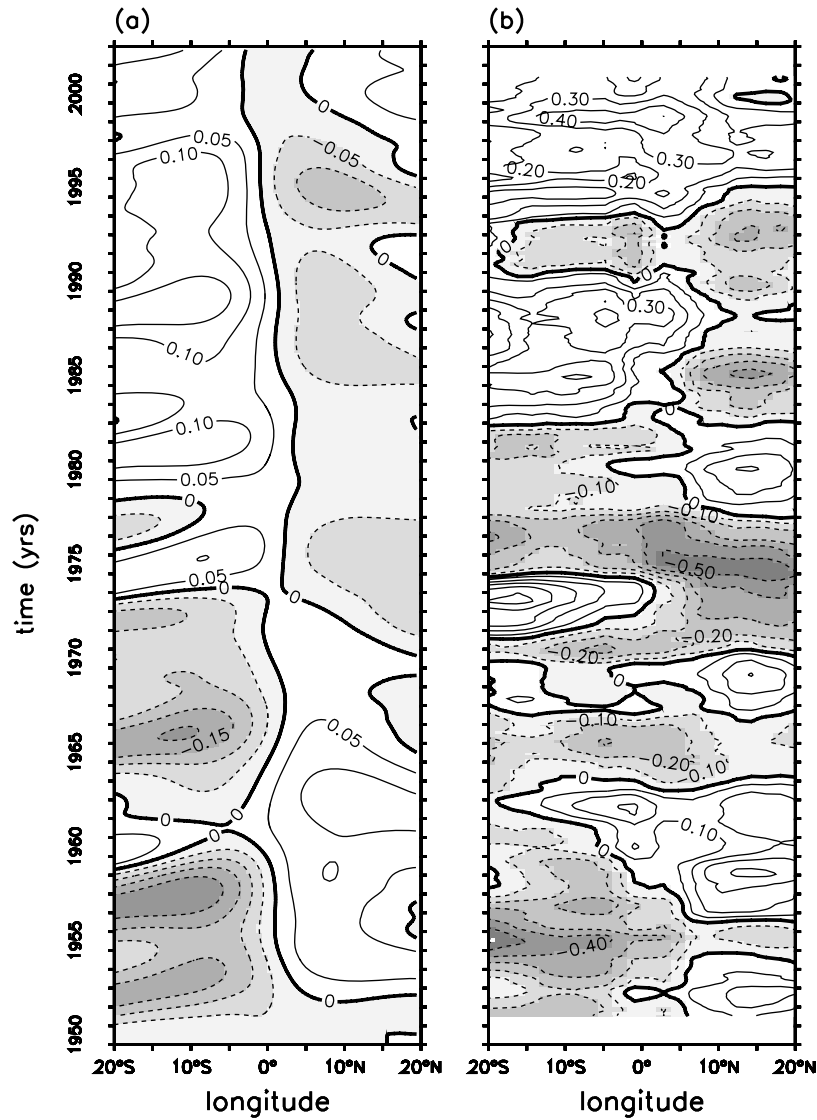


Figure 12. Exp-6: Latitude-time evolution of the (a) simulated versus (b) observed SST anomaly (NCAR/NCEP reanalysis data; Kalnay et al., 1996), both averaged zonally between 80°W and 20°E. The observed SSTA is the three-year running mean.

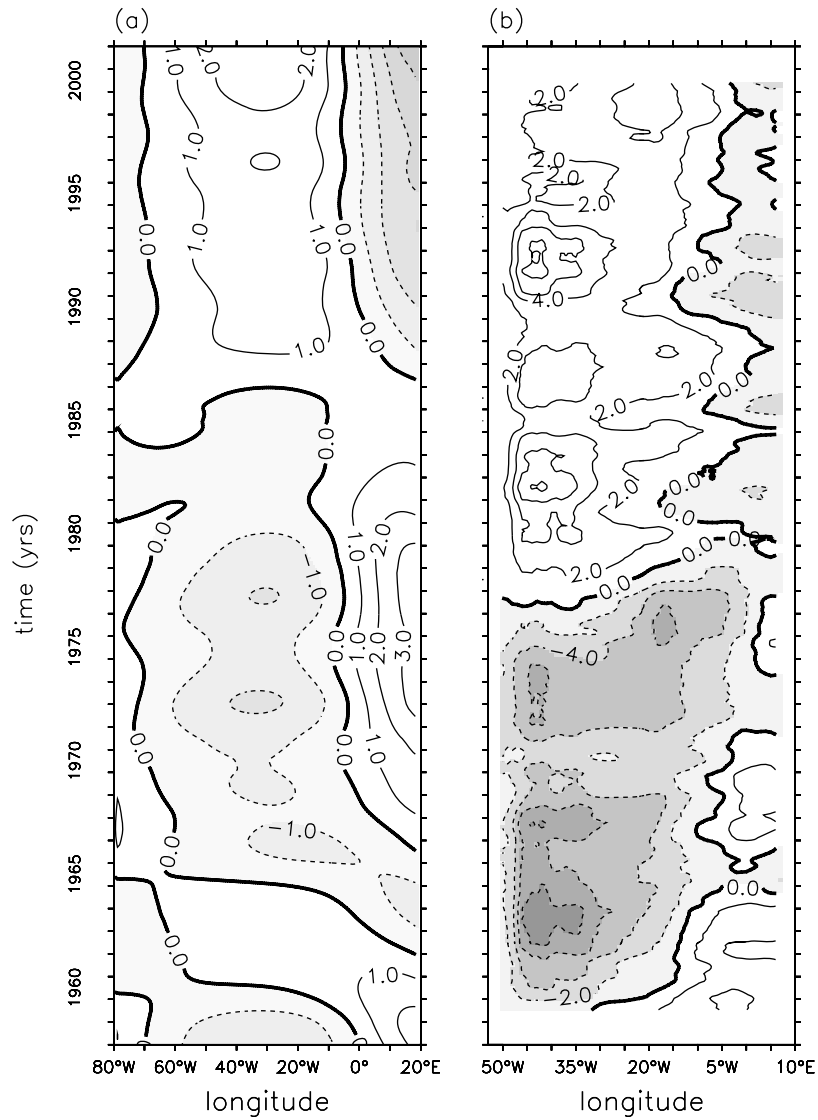


Figure 13. Exp-6: Longitude-time structure of (a) the simulated equatorial mixed layer depth, and (b) the 20°C isotherm in the equatorial Atlantic obtained from the HYCOM run. In both cases, the depth anomalies are averaged between 5°S and 5°N. The HYCOM output is the three-year running mean.

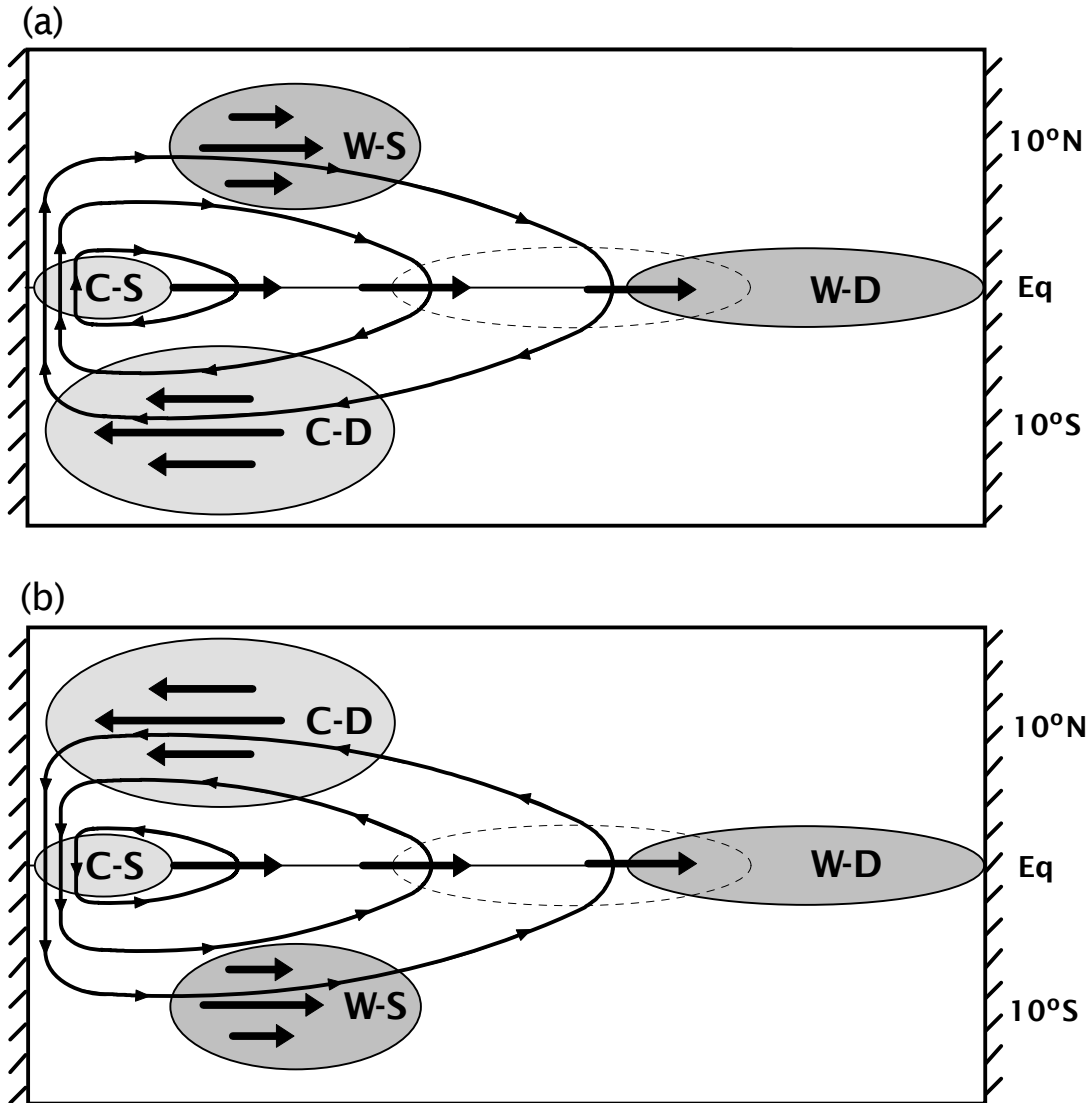


Figure 14. Sketch of the mechanism by which the positive zonal SST gradient is induced along the equator during (a) the positive and (b) negative phases of the Atlantic dipole oscillation. Thicker arrows indicate wind perturbations associated with the dipole oscillation. Dark shades are used for warm SST anomalies and light shades for cold SST anomalies. W-D represents a warm and deep anomaly; W-S a warm and shallow anomaly; C-D a cold and deep anomaly; and C-S a cold and shallow anomaly. Closed circuits represent cross-equatorial gyre circulation that brings the tropical surface water toward the equator. This gyre circulation supplies cold water in the western boundary layer and warm water in the Sverdrup interior during both the positive and negative phases of the dipole oscillation. The warm equatorial SSTA is then shifted to the east and intensified as a result of the Bjerknes feedback, thus, producing a permanent Atlantic-Niño condition.